

ABSTRACT

Title of dissertation: NONLINEAR DYNAMICS
 IN BIOLOGICAL SYSTEMS:
 ACTIN NETWORKS AND
 GENE NETWORKS
 Andrew Pomerance, Doctor of Philosophy, 2009

Dissertation directed by: Professor Wolfgang Losert
 Department of Physics

Two problems in biological systems are studied: (i) experiments in microscale deformations of actin networks and (ii) a theoretical treatment of the stability of discrete state network models of genetic control.

In the experiments on actin networks, we use laser tweezers to locally deform actin networks at the micron scale as a model of the action of molecular motors and other cellular components, and we image the network during deformation using confocal microscopy. Using these tools, we observe two nonlinear effects. The first observation is that there are two time scales of relaxation in the network: the stress induced by deformation relaxes rather quickly, however, the strain relaxes at a different rate. Additionally, upon removing the deforming force, the initial rate at which the strain relaxes seems to be independent of the amount of stress still in the network. The second observation is that large deformations are irreversible, and imaging the network implies that a large-scale snapping event seems to accompany this irreversibility.

In the theoretical treatment of gene networks, we focus on the stability of their dynamics in response to small perturbations. Previous approaches to stability have assumed uncorrelated random network structure. Real gene networks typically have nontrivial topology significantly different from the random network paradigm. In order to address such situations, we present a general method for determining the stability of large Boolean networks of any specified network topology and predicting their steady-state behavior in response to small perturbations. Additionally, we generalize to the case where individual genes have a distribution of ‘expression biases,’ and we consider non-synchronous update, as well as extension of our method to non-Boolean models in which there are more than two possible gene states. We find that stability is governed by the maximum eigenvalue of a modified adjacency matrix (λ_Q), and we test this result by comparison with numerical simulations. We also discuss the possible application of our work to experimentally inferred gene networks and present approximations to λ_Q in several cases.

NONLINEAR DYNAMICS IN BIOLOGICAL SYSTEMS:
ACTIN NETWORKS AND GENE NETWORKS

by

Andrew Pomerance

Dissertation submitted to the Faculty of the Graduate School of the
University of Maryland, College Park in partial fulfillment
of the requirements for the degree of
Doctor of Philosophy
2009

Advisory Committee:
Professor Wolfgang Losert, Chair/Advisor
Professor Michelle Girvan
Professor Brian Hunt
Professor Doron Levy
Professor Edward Ott

Table of Contents

List of Tables	iv
List of Figures	v
1 Introduction to Cell Biology	1
1.1 The Cytoskeleton and Actin	2
1.1.1 Actin: The molecule, the filament, the legend	3
1.1.2 Actin in the Cell	6
1.1.3 Purified Actin	8
1.2 The Nucleus, DNA, and Gene Networks	9
1.2.1 From DNA to Protein	9
1.2.2 Transcription Factors and Gene Networks	13
2 Relaxation of locally deformed actin networks	15
2.1 Introduction	15
2.2 Materials and Methods	17
2.2.1 Sample preparation	17
2.2.2 Green laser tweezer experiments	18
2.2.3 Direct Imaging of Actin Networks	19
2.3 Results	19
2.3.1 Small Deformations	19
2.3.2 Large Deformations are Irreversible	23
2.4 Discussion	26
3 Stability of Boolean Models of Genetic Networks	28
3.1 Introduction	28
3.2 Model	35
3.3 Statistical Methods	42
3.4 Results	44
3.4.1 In-/Out-degree Correlations and Heterogeneous Time Delay	45
3.4.2 Assortativity/Disassortativity	46
3.4.3 Motifs	46
3.4.4 Application to <i>S. cerevisiae</i>	47
3.4.5 Heterogeneous Correlated Sensitivities	47
3.4.6 Community Structure	48
3.4.7 Non-Boolean Models	49
3.5 Discussion	49
4 Approximating λ_Q	53
4.1 Introduction	53
4.2 Markovian Networks	57
4.3 Evaluation of λ_Q	59
4.3.1 The Effect of Nodal Correlations	59

4.3.2	Assortativity	60
4.3.3	Community and Bipartite Structure	62
4.4	Numerical Tests	65
4.4.1	First-order Approximation	65
4.4.2	Assortativity	66
4.4.3	Community Structure	70
4.5	Conclusion	70
A	Actin Purification	73
A.1	Extracting Polymerized Actin	73
A.2	Depolymerization and Final Purification	74
B	Overview of Microscopy and Image Processing Techniques	76
B.1	Laser Tweezers	76
B.1.1	General Principles	76
B.1.2	Holographic Laser Tweezers	79
B.2	Confocal Microscopy	80
B.3	Image Analysis	82
B.3.1	Particle Tracking	82
B.3.2	Particle Imaging Velocimetry	82
C	Technical Notes on Boolean Networks	84
C.1	Transient Evolution	84
C.2	Finite-Size Effects	85
C.3	Comparison of Mean-field Eigenvalue Approximations with Exact λ_Q	89
C.4	Application to the Regulatory Network of <i>S. cerevisiae</i>	90
	Bibliography	92

List of Tables

C.1 Comparison between criticality conditions evaluated directly from Q and from the approximate theory.	91
---	----

List of Figures

1.1	Endothelial cells with cytoskeletal components fluorescently labeled. The actin cortex has been labeled with a red fluorescent protein, the microtubules have been labeled with green fluorescent protein, and the nucleus has been labeled blue. Image Source: National Institutes of Health, http://rsb.info.nih.gov/ij/images/	3
1.2	Image of G-actin monomer and the double helix structure of F-actin. Image Source: National Library of Medicine, http://ghr.nlm.nih.gov/	4
1.3	Illustration of the polymerization of actin.	5
1.4	Illustration of the action of some actin binding proteins.	7
1.5	Illustration of the process by which DNA encodes the instructions for making proteins. DNA is first transcribed into mRNA, which is then translated into an amino acid sequence that forms the final product protein. Image Source: National Institutes of Health, http://stemcells.nih.gov	12
2.1	Three small-strain experiments plotted together. The relaxation speeds are very similar and the bead returns close to its original position. <i>Inset.</i> Schematic or image showing the channel formed behind the bead after being displaced.	20
2.2	The amount of relaxation vs. the total pulling time for pulls that were held at their destination (squares) and slow, constant pulls (circles).	21
2.3	(a) Sample trajectories after holding the bead at its destination for 1, 5, 10, and 50 seconds. The beads were pulled $4 \mu\text{m}$. The amount of recoil decreases with increasing hold time. The initial speed of the recoils are the same for a short time. The beads recoil back to their equilibrium position at approximately $4 \mu\text{m/s}$	22
2.4	The relaxation distance vs. the initial displacement. The dashed line corresponds to perfect recoil in the case of a purely elastic material. Viscoelastic materials should exhibit an increasing amount of recoil with increased displacement, however there is a maximum in the relaxation distance at 4 microns. This suggests some sort of damage to the network for deformations larger than 4 microns.	23

2.5	Confocal images with the deformation field around the pulled bead superimposed, as calculated by PIV. Two times are shown: (a) when a significant amount of actin is entrained behind the bead and (b) when the entrained actin snaps away from the bead while it is still being pulled.	24
2.6	Extracted flow speed in the direction of the bead pull from PIV along the direction of pull. The bead position is illustrated with a vertical dashed line in each panel. Panels (b) and (c) correspond to Figs. 2.5(a)-(b), and show the flow speed vs. position along the pull. Panel (a) is from before a significant amount of actin is entrained with the bead. As can be seen, after the snapping event, the actin retracts from the bead at $\sim 0.5\mu\text{m/s}$. After the bead is released, there is a general relaxation, the peak of which is approximately the same as the retraction from snapping.	25
3.1	(a) \bar{y} vs. q for three networks with different largest eigenvalues ($\lambda \approx 5.5, 3.4, 2.3$), both with uniform delay on all links $\tau_{ij} = 1$ (closed markers) and with half the links having increased delay of $\tau_{ij} = 10$ (open markers). The solid curves correspond to the prediction \bar{y} (defined in Eq. (3.17)) obtained by simulating Eq. (3.6). The downward vertical arrows correspond to $q_{crit} = 1/\lambda$ for each of the three networks. (b) \bar{y} vs. q for three networks with different assortativities. (c) \bar{y} vs. q for networks with added feedforward motifs, with an illustration of the feedforward motif (inset). (d) \bar{y} vs. q_0 for networks with maximum correlation (circles) and minimum correlation (squares) between $K_i^{in} K_i^{out}$ and q_i , where q_i is drawn from a uniform distribution centered at q_0 with width 0.1. (e) \bar{y} vs. $\theta_{\cap}/(\theta_{\cup} + \theta_{\cap})$ for networks with community structure, where the two communities have $q_a = 0.5$ and $q_b = 0.1$. (f) \bar{y} vs. p_0 for a network where each node can take one of $S_i = 4$ possible states. p_0 is the probability that a zero appears in the truth table output; the remaining three symbols appear with equal probability.	50
4.1	$\lambda_Q/\langle d \rangle$ vs. $\langle qd^{in}d^{out} \rangle/\langle d \rangle^2$ for networks of size $N = 10^4$ with no assortativity and $\langle d \rangle = 100$ (filled markers) and $\langle d \rangle = 10$ (open markers). For both values of $\langle d \rangle$, three values of η are considered: maximal (circle), neutral (triangle) and minimal (squares). Each marker is the average of 10 networks, and the solid line is the theoretical prediction, $\lambda_Q/\langle d \rangle = \langle qd^{in}d^{out} \rangle/\langle d \rangle^2$	67

4.2	(a) $\lambda_Q/\langle d \rangle$ vs. ρ_Q for a network of size $N = 10000$ and average connectivity $\langle d \rangle = 10$ (circles) and $\langle d \rangle = 100$ (squares). Each marker is the average of 10 networks. (b) $\lambda_Q/\langle d \rangle$ vs. $\hat{\lambda}_Q^{(0)}\rho_Q/\langle d \rangle$ for networks with structural assortativity of 0.8 (circles), 1.0 (triangles), and 1.2 (squares) of size $N = 10000$ and average connectivity $\langle d \rangle = 10$ (open markers) and $\langle d \rangle = 100$ (filled markers).	69
4.3	λ_Q vs. q_- for networks of size $N = 10^4$ with two equal groups of varying type: two completely separated components ($p_x = 0$, circles), strong community structure ($p_x = p_0/2$, squares), no group structure ($p_x = p_0$, upward pointing triangle), and strong bipartite structure ($p_x = 2p_0$, downward pointing triangle). Each marker is the average of 10 networks, and the solid curves are the theoretical predictions of Eq. (4.40).	71
B.1	Illustration of lateral optical trapping. (a) When the particle is displaced in the trap to the left, the force resulting from refracting light to the right, F_1 , is smaller than the force resulting from refracting light to the left, F_2 . The result is a net restoring right, F_{net} . (b) When the particle is in the center of the trap, F_1 and F_2 balance each other, so that the net force is down, which is balanced by radiation pressure. Image courtesy Wikipedia entry on Optical Tweezers. . . .	78
B.2	Schematic beam path in a confocal microscope. The laser illuminates the sample, which excites fluorescence by the probes in the sample. The fluorescent light is collected by the object and focused. However, some of the fluorescent light is emitted by probes outside the focal plane. This light is blocked by a pinhole aperture in front of the photomultiplier tube, which detects the light. Image courtesy Olympus Corporation, http://www.olympusfluoview.com/theory/index.html	81
C.1	(a) Evolution of the Hamming distance between two initial conditions for a typical network of size $N = 1000$ and $\epsilon = 0.01$ for various values of the sensitivity and uniform delay $\tau_{ij} = 1$. (b) Evolution of the Hamming distance between two initial conditions for a typical network of size $N = 1000$, $q = 0.5$, and $\epsilon = 0.01$. Results are shown for a network with $\tau_{ij} = 1$ for all links (solid curve) and with $\tau_{ij} = 10$ on 0.1 (dashed curve) and 0.5 (dotted curve) of the links.	86

C.2	The steady-state fractional Hamming distance h/N for (a) $N = 10^3$ and (b) $N = 10^4$ as a function of the sensitivity q for various values of ϵ , both in the frozen case (filled symbols) and the annealed case (open symbols). The largest eigenvalue of this network's adjacency matrix is $\lambda \approx 5$. While the theory does not depend on the value of ϵ , finite-size effects cause a dependence on the number of flipped bits. The inset to (a) shows a histogram of measured Hamming distances at $q = 0.4$ and $\epsilon = 0.01$ (up arrow).	88
C.3	\bar{y} vs. q , calculated from Eq. [17], for the published regulatory network of <i>S. cerevisiae</i> [35]. The network undergoes a transition from stable to unstable behavior at $q_{crit} = 1/\lambda = 0.40$	90

Chapter 1

Introduction to Cell Biology

This dissertation presents results from two different projects on problems in biophysics. Chapter 2 discusses results of experiments on microscale deformations of entangled solutions of purified actin, an important component of the cytoskeleton. Chapters 3 and 4 deal with theoretical results on models of gene networks, which control the expression of RNA and the amount of proteins in the cell. Consequently, this chapter is a brief overview of cell biology in order to give biological context to and motivate the results of later chapters; however, the actual systems under study are rather isolated from the complicated biological processes described here.

Cells are sacks of organic material separated from their environment by a wall or membrane, usually constructed of a bilayer of lipids. The structures inside the sack range from a few strands of DNA and small structures consisting of a few molecules in the case of bacteria, to highly compartmentalized, large structures consisting of hundreds of proteins in eukaryotic cells. Broadly speaking, however, eukaryotic cells consist of two parts, the nucleus and the cytoplasm. The nucleus contains all the DNA necessary to produce the proteins that make up the cell and will be the subject of Sec. 1.2. The cytoplasm consists of everything else: mitochondria (metabolic structures), vesicles (small sacks used for transferring material into, out of, or within the cell), signaling proteins, etc. In particular, we are concerned with

the cytoskeleton, the cellular scaffolding.

1.1 The Cytoskeleton and Actin

The cytoskeleton is the key material component of a cell that gives cells their shape and produces forces used for locomotion. The cytoskeleton is highly dynamic: the structures of the cytoskeleton are usually assembled and disassembled many times a minute as a cell migrates through its environment, and the filaments that comprise it are constantly growing and shrinking, even in a resting state. Molecular motors traverse filaments of the cytoskeleton, to produce forces on the cell's environment or to move material within the cell.

The cytoskeleton is, essentially, a polymer gel consisting of three types of polymers of varying length and stiffness (see Fig. 1.1):

1. Actin is the smallest (6 nm diameter) and most flexible filament. It tends to concentrate near the cell membrane and produces protrusions used in motility and binds to cellular anchors in the substrate. It also plays a key role in producing the tension in muscular contraction.
2. Intermediate Filaments are larger (10 nm), stiffer filaments that shape and place the nucleus and other organelles in the cytoplasm.
3. Microtubules are the largest (23 nm) and stiffest filaments of the cytoskeleton. They form the cilia and flagella (hair- and tail-like structures on the cell surface used for navigating water environments) and the structures used in cellular division.

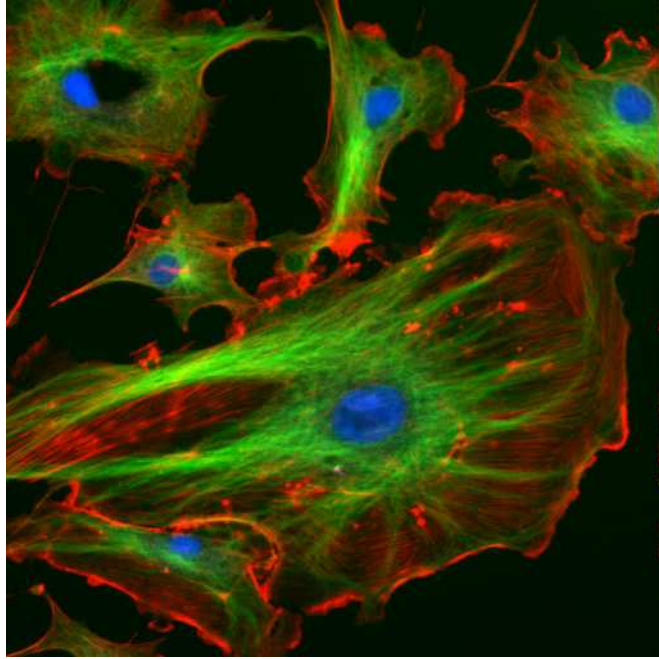


Figure 1.1: Endothelial cells with cytoskeletal components fluorescently labeled. The actin cortex has been labeled with a red fluorescent protein, the microtubules have been labeled with green fluorescent protein, and the nucleus has been labeled blue. Image Source: National Institutes of Health, <http://rsb.info.nih.gov/ij/images/>

Since the experiments of Chapter 2 focus on actin, the following subsections give more background on those filaments.

1.1.1 Actin: The molecule, the filament, the legend

An excellent review of actin and its binding proteins is Ref. [1], which is summarized in this subsection. Monomeric actin (see Fig. 1.2), also known as G-actin, is a 43 kDa globular protein with dimensions $67 \times 40 \times 37 \text{ \AA}$. G-actin has

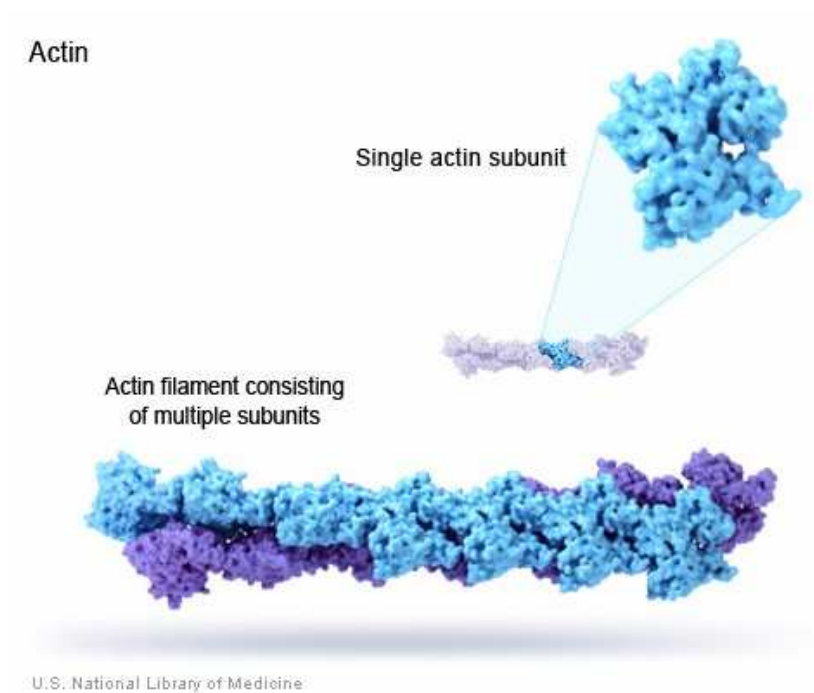


Figure 1.2: Image of G-actin monomer and the double helix structure of F-actin.

Image Source: National Library of Medicine, <http://ghr.nlm.nih.gov/>

four subdomains, which leave a deep fold in the center of the molecule, which binds a nucleotide, either ATP (forming ATP-actin) or ADP- P_i (forming ADP-actin). G-actin also forms a complex with divalent cations Mg^{2+} or Ca^{2+} ; if magnesium is bound, G-actin binds more tightly with the nucleotide.

G-actin solutions above the critical concentration polymerizes to form F-actin, which is illustrated in Fig. 1.3. The presence of K^+ and Mg^{2+} lowers the critical concentration by an order of magnitude, and it is under these conditions that most in vitro studies of actin occur. F-actin filaments have polarity, the two ends being barbed and pointed. Polymerization proceeds in three steps: (i) dimerization, where two G-actin molecules are loosely bound and unlikely to elongate; (ii) trimerization,

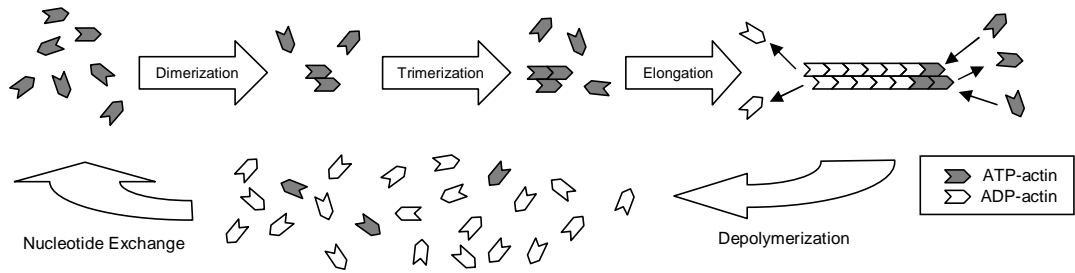


Figure 1.3: Illustration of the polymerization of actin.

where a third G-actin monomer is bound to a dimer to form a stable trimer; and (iii) elongation, where additional G-actin monomers are added to the filament. Additionally, during the elongation phase, there is a small amount of disassembly at both ends of the filament leading to a small amount of G-actin in solution.

While elongation can occur on both ends, monomers are predominantly added to the barbed end (the critical concentration at the barbed end is an order of magnitude lower than at the pointed end). Filament assembly occurs almost exclusively with ATP-actin, but, once in the filament, the ATP is normally hydrolyzed such that the majority of actin in the filament is ADP-actin (see Fig. 1.3). This step consumes the energy stored in ATP and leads to polymerization being not entirely reversible since G-actin cannot rephosphorylate ADP; however, in monomer form, G-actin can easily swap its bound nucleotide to convert ADP-actin to ATP-actin.

Because of its crucial role in the cytoskeleton, actin has perhaps the most highly preserved structure of all proteins (i.e., most eukaryotic cells have the same actin to a large degree). Additionally, the genes that code for actin production have an unusual number of duplicates to mitigate the effects of possible mutations. As a

result, there are very few disorders associated with actin dysfunction, but those few are usually fatal.

1.1.2 Actin in the Cell

The ‘actin cortex’ in most cells is a layer of bound and cross-linked actin filaments that lies just beneath the lipid membrane of the cell, and this cortex gives cells their unique shapes and for the most part determines their elastic properties. Another important function of actin is to produce and transmit forces used for motility. Many cells ‘walk’ across surfaces in order to find food (such as single-celled amoebae) or perform other functions (such as white blood cells hunting down invading pathogens). In many cases, the cell will extend structures in the direction of travel (such as pseudopodia or filopodia), anchor that protrusion to the substrate (through the assembly of focal adhesions), and retract the trailing edge of the cell (through stress fibers that link focal adhesions). Actin plays a crucial role in all three processes: forces generated by actin polymerization deform the membrane and create the prehensile structure; focal adhesions, transmembrane complexes of proteins that bind to the surface, are anchored to the actin cortex; and stress fibers, which contract to retract the trailing edge of the cell, are bundled actin fibers that are pulled by molecular motors. Thus actin is an important component of the cell’s motility machinery.

In order to accomplish all these functions, there is a panoply [1] of actin-binding proteins that destroy, shape, and rebuild the actin cortex. For instance,

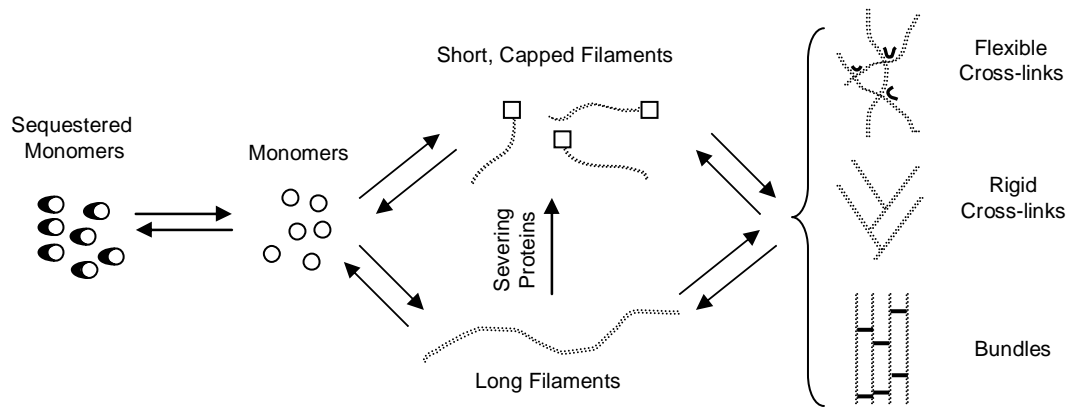


Figure 1.4: Illustration of the action of some actin binding proteins.

here is a small sample of some actin-binding protein functions, which are illustrated in Fig. 1.4:

1. Sequestering proteins (e.g., cofilin, thymosin and profilin) bind to actin monomers to prevent polymerization, and in some cases speeds depolymerization (e.g. cofilin);
2. Capping proteins (e.g., CapZ, tropomodulin, and gelsolin) bind to the growing end of an actin filament to prevent further growth or degradation;
3. Severing proteins (e.g., gelsolin) cut long actin filaments into shorter filaments;
4. Cross-linking proteins bind actin filaments together, sometimes flexibly (e.g., α -actinin), in well-defined patterns (e.g., Arp2/3), or into bundles (e.g. fascin, or, under certain conditions, α -actinin).

1.1.3 Purified Actin

Actin is present in most eukaryotic cells, and could be purified from almost any one. Muscle cells, however, are the best source of actin, since muscles are essentially large contractile actin bundles (much like the stress fibers on a subcellular-level). In the experiments discussed below, actin was prepared from rabbit muscle by the method of Spudich and Watt [6], which is briefly summarized here.

Actin is purified from rabbit muscle in three phases. In the first phase of actin preparation, rabbit muscle is treated with acetone to dissolve the lipid membranes surrounding the cells and make the actin soluble. This muscle acetone powder can be stored at -20 deg C for up to two years. The next phase of preparation extracts actin from the acetone powder by dissolving the actin in buffers. This yields polymerized actin, which must be depolymerized in the third phase by dialysis against buffer without polymerizing agents. Appendix A details the steps to extract polymerized actin from muscle acetone powder.

Purified actin is polymerized by the addition of K^+ and Mg^{2+} ions and ATP, and at high enough concentrations, actin forms an entangled polymer solution without crosslinks. The rheology of purified entangled actin solutions, summarized in Chapter 2, has been extensively studied yet many important questions remain. One such question is how entangled actin solutions respond to deformations at the subcellular level, such as those that might be experienced by a motile cell. Chapter 2 also presents experiments that actively deform actin solutions and reports observations about the relaxation of deformations.

1.2 The Nucleus, DNA, and Gene Networks

Changing gears to motivate the results of Chapters 3 and 4, this section reviews the nucleus. The nucleus is colloquially known as the ‘brain’ of the cell since all instructions for making the many proteins that make up a cell are encoded in DNA located in the nucleus.

1.2.1 From DNA to Protein

Deoxyribonucleic acid (DNA) molecules are long, double-stranded polymers composed of nucleic acids (also known as DNA bases), which come in four varieties: adenosine, cytosine, guanine, and thymine. The two strands are complementary to each other, i.e. the bases of one strand are bound to the bases of the other in base pairs: adenosine in one strand binds only to thymine in the other, and cytosine binds only to guanine in the other. Thus one strand, the coding strand, contains the instructions for assembling a protein; the other, the template strand, is merely its complement and encodes the same information.

A single double-stranded DNA polymer contains many genes, which are subsections of DNA that encode a single protein. Many genes comprise a chromosome, which is a complex of DNA and histones, proteins around which DNA is tightly wound in order to conserve space in the nucleus. There are usually multiple chromosomes in an organism: human cells have 23 chromosomes, while horses have 32 and dogs have 39. These chromosomes are then packaged in the nucleus with various structural and control proteins.

Ribonucleic acid (RNA) is a related, single-stranded molecule composed of similar bases to DNA, with the substitution of uracil for thymine. RNA comes in many forms for different uses in the cell, many of which are still poorly understood. Three forms that have well-established roles, however, are messenger RNA (mRNA), transfer RNA (tRNA), and ribosomal RNA (rRNA), which will be explained below.

In order to produce a protein from DNA, the cell performs two broad steps, illustrated in Fig. 1.5: (i) transcription, the copying of DNA into mRNA, a single-stranded copy of the bases encoding a single gene; and (ii) translation, the assembly of proteins from the mRNA instructions. During transcription, the DNA is unwound from the histone and a segment of double-stranded DNA is exposed to transcription molecules. RNA polymerase (RNAP), the enzyme that produces mRNA, is recruited to the DNA molecule by transcription factors (the subject of Sec. 1.2.2 below), and initiates transcription by unwinding the DNA and separating the two strands. RNAP then walks down the template strand, closing the DNA behind it and opening the DNA in front of it. At each base site on the DNA molecule, RNAP recruits the complementary RNA base and binds it to the elongating mRNA molecule. RNAP continues in this way until it is terminated through a variety of mechanisms, and an mRNA copy of the coding strand leaves the nucleus to be transcribed in the cytoplasm.

Before describing translation, a brief overview of how information is encoded by DNA is in order. The fundamental unit of translation is the codon, a sequence of three bases on the mRNA molecule to be translated. Each of the 64 (4^3) codons encode a single amino acid, the subunit from which proteins are built: this is the

genetic code. There are only about 20 amino acids, so there is significant degeneracy in the code, but four codons have special meaning. There is one start codon that initiates translation (and also codes for the amino acid methionine) and three stop codons that terminate it. Transfer RNA, which is RNA bound to an amino acid, exposes a 3 base *anti*-codon, which is the complement of a codon on the mRNA molecule to be translated.

The main actors in translation are ribosomes, fairly large (20 nm) complexes of many proteins (see Fig. 1.5) and ribosomal RNA, that have two codon-sized binding sites. A ribosome binds to an mRNA strand to be translated at the start codon in the first binding site. A tRNA molecule, bound to methionine and with anti-codon complementary to the start codon, enters the first binding site. Another tRNA molecule, bound to its amino acid and with anti-codon complementary to the second codon in the sequence, enters the second binding site. The ribosome then binds the two amino acids together, and releases the tRNA molecule in the first binding site. The ribosome slides the mRNA molecule down one codon such that the attached tRNA now occupies the first binding site. In this way, the protein is elongated: complementary tRNA molecules with bound amino acids enter the second binding site, the ribosome binds the amino acids together and slides down the mRNA molecule. This continues until a stop codon enters the second binding site, whereupon the ribosome releases the tRNA molecule and amino acid chain for further processing to become a functional protein.

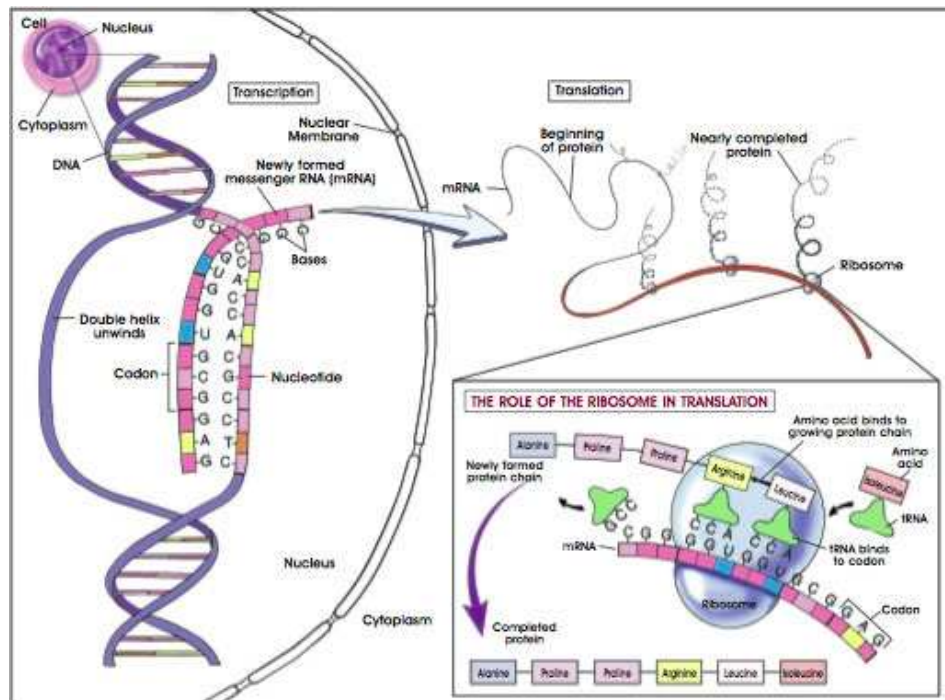


Figure 1.5: Illustration of the process by which DNA encodes the instructions for making proteins. DNA is first transcribed into mRNA, which is then translated into an amino acid sequence that forms the final product protein. Image Source: National Institutes of Health, <http://stemcells.nih.gov>

1.2.2 Transcription Factors and Gene Networks

The story of the previous section, of course, is only the coarsest approximation of DNA transcription and translation. The previous discussion implies that the process is open loop, such that DNA is being transcribed without any control; this cannot be the case since differentiated cells in organisms, while sharing the same DNA, have vastly different constitutions. Actin composes up to 20% of all protein in muscle cells, but makes up significantly less in neurons. Conversely, neurons are constantly producing neurotransmitters while muscles produce little, if any. Thus, cells must control the production of protein, and one important mechanism is through transcription factors.

Transcription factors (TFs) are proteins that directly bind to DNA and control expression (i.e., the transcription and translation) of a gene, and a good introduction is Ref. [2], summarized here. In a chromosome in front of most genes, there is a promoter region. This promoter region is a sequence of DNA bases that are not transcribed into mRNA for translation, but serve as a segment of DNA where TFs and other translation mediating proteins can bind. In general, each gene has a unique promoter region (although closely related or duplicate genes may have very similar promoter regions). Therefore, at a minimum, TFs contain a DNA-binding region, which binds to a specific sequence of DNA and determines the target of the TF. Then, depending on the function of the TF, there may be a region that recruits other proteins to initiate transcription, i.e., the TF can activate the gene. Conversely, the TF may contain domains to block transcription of the gene, in

which case the TF represses the gene. Other regions of the TF may allow binding of signalling proteins or other modification to activate or deactivate the activity of the TF itself. Thus these proteins allow for significant control of DNA expression.

The action of transcription factors forms a complex web of interactions among the different genes, proteins, and other chemical species in a cell. One way to conceptualize these interactions is with a gene network: each node in the network is a gene, and an edge is drawn from one node to another if expression of the source gene affects expression of the destination gene.

One important, albeit significantly simplified, model of gene networks is the Boolean network model, where each gene takes on one of two states, on or off. This model, which will be fully explained in Chapter 3, includes rules for the dynamic evolution of every gene state. An important property of these networks is their stability; i.e., whether perturbations in the states of a small number of genes spread to the entire network or quickly die out. Chapter 3 presents a method for determining the stability of a given network, and Chapter 4 analyzes the effects of topological properties on network stability.

Chapter 2

Relaxation of locally deformed actin networks

2.1 Introduction

Actin is an important semi-flexible, double-stranded bio-polymer that is found in all eukaryotic cells. Actin filaments are the main component of the cytoskeleton, which gives cells their shape and transduces the forces required for motility [3, 4].

The actin network is an active component which generates forces for cell deformation and motion through two key processes. Actin polymerization can push the leading edge of cells forward, and is guided by a protein machinery that guides the location of actin polymerization and filament disassembly. Myosin motors drive contraction of the actin network, a process for example utilized in retraction of the uropod of motile cells. The mechanical properties of this active biopolymer network are of great interest, since cell mechanical properties play a role in many diseases. For example, metastasis of cancer cells involves pushing of cells through their environment toward the bloodstream [5].

In motile cells, the actin network experiences significant stresses and deformations [12], which have been shown to increase the apparent stiffness of this prestressed actin network by nearly 100-fold [25]

In this study we investigate experimentally intermediate scale deformations and relaxations of *in vitro* of such semiflexible actin network. Localized deformations in

such self assembled actin networks are generated by moving beads that are embedded in the actin network. We focus in this study on the relaxation of these deformations. In particular we study the transition from reversible to irreversible deformations.

The material properties of actin have been extensively studied, both for its importance in cell biology and as an interesting polymer science question. Actin is a semi-flexible polymer, i.e. its persistence length is on the order of the filament size. This is in contrast to most commercially important polymers, flexible chain polymers, which are much longer than their persistence length. Various techniques to measure $G^*(\omega)$ have been used in the past, including macroscale rheometry [13, 14, 37], passive single- and multi-point [15, 16, 37] microrheology, magnetic-bead active microrheology [17, 18, 19], and laser tweezer active microrheology [20]. These experiments have lead to the discovery of several novel properties of semiflexible networks that are in contrast to the properties of polymers with flexible chains. For instance, there is a rubber plateau where the actin solution exhibits 100 Pa shear modulus plateau at 0.1% volume density, compared to 1 Pa in a polystyrene solution of comparable volume density [22, 23]. There is also significant strain-hardening in actin solutions [24, 25], which is shown to be a direct consequence of the large bending energy and long persistence length [26]. Studies of the creep response of actin show the existence of a short-time regime where $x(t) \propto t^{3/4}$ [18, 27], corresponding to the high-frequency dependence of the modulus $G \propto \omega^{-3/4}$ [28, 29]. At long times, the creep response is strictly viscous, $x(t) \propto t$. Additionally, there is an intermediate regime where $x(t) \propto t^{1/2}$ which is explained as an osmotic restoring force generated by filament pile-up [30].

We study localized deformations of *in vitro* actin networks as a model for the localized strains found in cells e.g. strains generated by molecular motors. Localized deformations in *in vitro* actin networks are generated by moving beads that are embedded in the actin network with a laser tweezer. We focus in this study on the relaxation of these deformations, and in particular on two non-linear effects. First, we study the effect of allowing stress to relax before releasing imposed strain and find that the strain relaxation rate is approximately independent of the remaining stress. We explain this finding in terms of entropic relaxations in the context of the tube model. Second, we study the transition from reversible to irreversible micro-scale deformations with increasing strain. Using fluorescence imaging we find that this transition is accompanied by a ‘snapping’ event with sudden local relaxations of the actin network, which we can measure with PIV and force measurements.

2.2 Materials and Methods

2.2.1 Sample preparation

Samples were prepared by addition of 0.01% by volume $1\mu\text{m}$ diameter silica beads to purified actin in Buffer A, and polymerization was induced by addition of PB. The polymerizing actin was placed into the sample chamber by pipette and sealed within 30 seconds. For experiments on the green laser tweezer system, the sample chamber consisted of a standard microscope slide with a hole drilled through it and sealed by two Number 2 microscope cover slips attached with nail polish, which held approximated $100\ \mu\text{L}$ of solution. For experiments on the confocal laser

tweezer, a small drop of actin was placed on a microscope slide and a Number 2 cover slip was placed over the drop. The actin samples were allowed to sit approximately 30 minutes before experimentation began and were used for up to 3 hours after initiating polymerization.

2.2.2 Green laser tweezer experiments

A Biorryx 200 (Arryx, Chicago, IL) holographic laser tweezer was used to perform bead-pulling experiments. The Biorryx 200 consists of a Nikon inverted microscope, a Spectra-Physics NdYAG laser, a spatial light modulator, and proprietary phase mask generation software. Beads were imaged at 60x magnification with a Photron Fastcam PCI at 125 frames per second. The thick samples allow us to minimize edge effects by studying only beads that are further than 50 μm from either surface. In order to impose a trajectory on the beads with a spatial light modulator, the optical trap is moved in a series of closely spaced steps aligned along the intended trajectory; the bead follows the steps of the trap quickly and then remains stationary until the next step. The stepping rate and step size determine the speed. The maximum rate at which traps can be set is the update rate of the SLM, 15 Hz, and the minimum step size is 194 nm. The minimum step size was used for all trajectories except for the fastest rates. Step sizes greater than 400 nm yield poor results, as the bead tends to fall out of the trap. The motion of embedded beads was measured using particle tracking software developed by Crocker et al. in [31].

2.2.3 Direct Imaging of Actin Networks

Actin network deformations and relaxations were imaged directly on a high speed spinning disc confocal microscope with built in laser tweezer. Briefly, the apparatus consists of a spinning disk confocal microscope that excites fluorescent probes that absorb blue laser and emit green light; the spinning disk confocal allows fast imaging of the sample. Additionally, there is also an infrared laser (1094 nm) used for trapping embedded microspheres. The tweezer on this system is moved by deflecting the beam with piezo-controlled mirrors. In order to image the actin network, the fluorescent speckle technique [36] was used, which involves adding actin bound to Alex Fluor 488 (Invitrogen, Carlsbad, CA) at low ratio (in our case 1:10).

While the direct tracing of filaments is not possible since the filaments are too close to each other, image sequences were analyzed using particle imaging velocimetry, which measures the average deformation in small regions of the sample by finding the best overlap between the region in the original image and a displaced region in the subsequent image [38].

2.3 Results

2.3.1 Small Deformations

Small Deformations are Reversible. Figure 2.1 shows representative trajectories from $2\mu\text{m}$ displacements, and the inset shows an image obtained on the confocal microscope of the strained network. The small perturbations relax consistently back

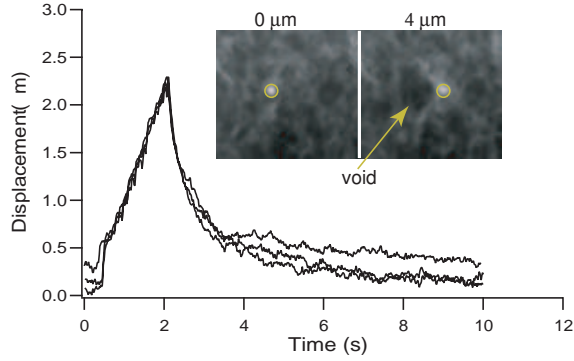


Figure 2.1: Three small-strain experiments plotted together. The relaxation speeds are very similar and the bead returns close to its original position. *Inset.* Schematic or image showing the channel formed behind the bead after being displaced.

to their equilibrium positions at roughly the same speeds, and this behavior is consistent up to 4 micron deformations (see Sec. 2.3.2), i.e. roughly four times the cage size. Additionally, by performing these experiments on the confocal microscope, we are able to image the effect of these deformations on the surrounding network. We see that there is a ‘channel’ behind the bead, with what appear to be extended filaments on either side.

Relaxation Amount Depends on Strain Time. We now investigate how the channel repairs itself while the network is held in a strained state. In a network that is locally strained by a $4\mu m$ displacement of an embedded bead, which is just at the transition to irreversible deformation, we measure how the relaxation of strain changes as a function of time the network was kept under strain in two ways. In the first, we hold the network in a strained state by keeping a bead at the end of its trajectory for a waiting time t_w . In the second, we strain the network at different

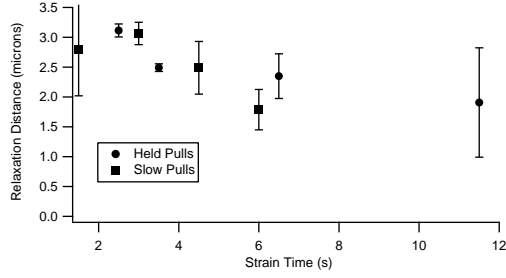


Figure 2.2: The amount of relaxation vs. the total pulling time for pulls that were held at their destination (squares) and slow, constant pulls (circles).

rates, such that the time the bead is moving, t_m varies by up to a factor of 4. In both cases, we expect the amount of recoil to decrease as a function of the total straining time $t_s = t_m + t_w$ due to the viscoelastic properties of actin solutions. In Figure 2.2, we see that to be the case, and that the channel heals over a timescale of approximately 10 seconds.

Relaxation Rate is Independent of Strain Time. In addition to the amount of relaxation, we expect the rate at which the bead initially relaxes should be strongly influenced by how long the bead was strained. However, this does not appear to be the case. In Figure 2.3(a) we show representative trajectories of beads after being pulled $4 \mu\text{m}$ and held for 1 to 50 seconds. We see that in almost all cases, the beads recoil at approximately $4 \mu\text{m/s}$; beads that are pulled slowly also recoil at roughly the same rate when finally released. By measuring the change in the bead's displacement in the trap, we can get measure the relative amount of force that is being applied to the bead by the actin network. We see in Fig. 2.3(b) that the bead settles more fully into the trap over a timescale of approximately one second, such

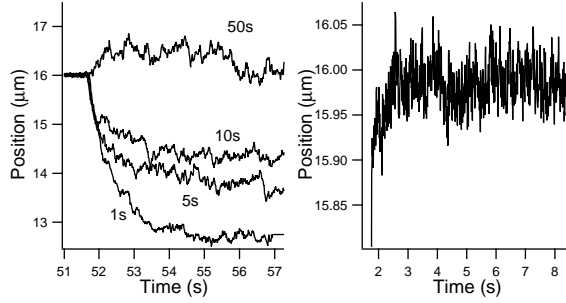


Figure 2.3: (a) Sample trajectories after holding the bead at its destination for 1, 5, 10, and 50 seconds. The beads were pulled $4 \mu\text{m}$. The amount of recoil decreases with increasing hold time. The initial speed of the recoils are the same for a short time. The beads recoil back to their equilibrium position at approximately $4 \mu\text{m/s}$ that the force is indistinguishable from noise. However, we still observe significant recoil even after $t_w = 10\text{s}$, which is significantly longer than the timescale over which the force relaxes. We interpret this to mean that the channel heals farthest away from the bead first, but the area behind the bead remains free of filaments for a significant amount of time. See the Discussion section for more details.

The observation of a relaxation rate that does not decrease with decreasing force can be understood in the context of entropic filament rearrangements within the tube model. Filaments in a gel are confined by their neighbors into a tube, within which the filament is free to fluctuate due to thermal or other excitations. Within such a framework, the dynamics of strain relaxation is governed by the time-scales of the interactions of filaments with their tubes. Other research indicated that filaments bunch up in front of the bead with concentration $c^* \sim l_p^{1/3} \xi^{8/3}$ [18], which implies a local cage size $\xi^* \sim 0.5 \mu\text{m}$. We propose that the speed at which an actin

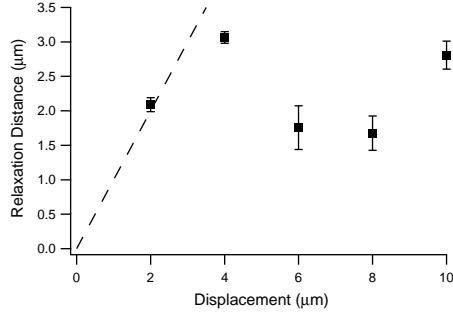


Figure 2.4: The relaxation distance vs. the initial displacement. The dashed line corresponds to perfect recoil in the case of a purely elastic material. Viscoelastic materials should exhibit an increasing amount of recoil with increased displacement, however there is a maximum in the relaxation distance at 4 microns. This suggests some sort of damage to the network for deformations larger than 4 microns.

gel relaxes a local strain is governed by the timescale that filaments collide with their neighbors (i.e., the entanglement time), and this has been shown to be about 0.1s [35, 37] at these concentrations. We note that the characteristic speed obtained by $\xi^*/\tau_e \sim 5\mu\text{m/s}$.

2.3.2 Large Deformations are Irreversible

Turning our attention to deformations larger than 4 microns, we see that these deformations do not relax back to their original conformation. In Fig. 2.4, we see that the amount of recoil drops sharply for deformations larger than 4 microns. Also, the error bars get significantly larger, which implies that the relaxation is not as uniform as for smaller displacements. This implies that there may be some damage being done to the network, and we use spinning disk confocal microscopy together

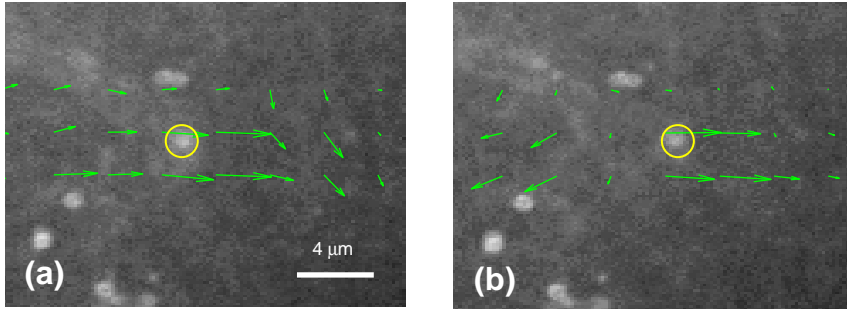


Figure 2.5: Confocal images with the deformation field around the pulled bead superimposed, as calculated by PIV. Two times are shown: (a) when a significant amount of actin is entrained behind the bead and (b) when the entrained actin snaps away from the bead while it is still being pulled.

with optical trapping to visualize the actin network while imposing strain in order to investigate the cause of the irreversibility of the deformation.

To the human eye, real-time movies of the actin network deformations also show snapping events far from the bead that suddenly appear after the bead is pulled a large distance. A semi-quantitative analysis of the actin network deformations with Particle Image Velocimetry (PIV) approaches reveals the deformation and relaxation fields of the actin network itself, and also captures the snapping event. Figure 2.5 shows the extracted velocity field for a time points just after the snapping event, and in Fig. 2.6 we plot the velocity profile of the extracted flow field for time points (a) long before, (b) right before, and (c) right after the snapping event. We see that just before the snapping event, actin behind the bead is entrained with its motion, but right after the snapping event, that entrained actin is moving away from the bead and relaxing towards its initial position.

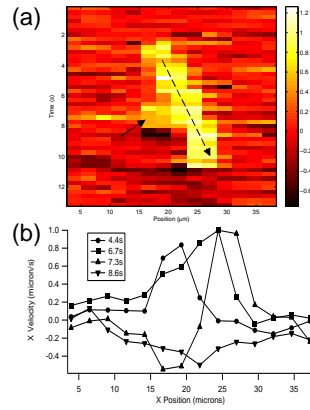


Figure 2.6: Extracted flow speed in the direction of the bead pull from PIV along the direction of pull. The bead position is illustrated with a vertical dashed line in each panel. Panels (b) and (c) correspond to Figs. 2.5(a)-(b), and show the flow speed vs. position along the pull. Panel (a) is from before a significant amount of actin is entrained with the bead. As can be seen, after the snapping event, the actin retracts from the bead at $\sim 0.5\mu\text{m/s}$. After the bead is released, there is a general relaxation, the peak of which is approximately the same as the retraction from snapping.

2.4 Discussion

In this paper we have presented results from two different experiments on microscale deformations of actin networks with laser tweezers. In the first experiment, we strained an actin network by moving beads trapped in the network and held it in the strained state. By holding it in this strained state, the stress in the network relaxes. However, when releasing the bead from the strained state, the rate at which the bead returns to its original position appears to be independent of the waiting time. We infer from this that the speed at which the actin network rearranges itself is independent of the stress in the network, and is perhaps driven by entropic processes rather than relaxing of bent filaments.

In the second experiments, we measured how far pulled beads recoiled towards their initial position. We observed that beads that are pulled less than about four microns tend to recoil fully back to their original position, and that the recoil is fairly uniform over different pulls in the same sample. Once the bead is pulled more than 4 microns, however, beads no longer recoil back to their original position. We imaged this experiment on a confocal microscope, that allows imagining of the strained network, and observed a snapping event in long bead pulls, which we hypothesize is the cause of the irreversible deformations in actin networks.

The recoil speeds and critical distance reported here should not be seen as representative of any distance scales relevant to actual cells; it depends on a variety of factors, such as concentration of the actin solution, the size of the tracer beads [32], cross-linking or other actin-related proteins [14], macromolecular crowding effects

[33], and surface chemistry of the beads [34]. In fact, the silica beads stick to the protein, which makes them less-than-ideal for these experiments. Carboxyl-modified polystyrene spheres do not, on the other hand, and tend to slide between filaments, which makes it the preferred material for tracers. However, the lower index of refraction makes for poor trapping on our system, so we were forced to use silica. Surprisingly, though, the same qualitative behavior is observed with carboxylated spheres. An interesting series of follow up experiments would determine the scaling of this behavior with sphere size. Larger spheres should entrain more filaments and thus be a less singular strain. It could be argued that the critical distance increases as any one entrained filament slipping or snapping causes an irreversible deformation. Conversely, one could argue that since more filaments are entrained, a single snapped filament would not have as much of an impact.

Chapter 3

Stability of Boolean Models of Genetic Networks

3.1 Introduction

Boolean networks have been extensively investigated as a model for genetic control of cells [39, 40]. In this model, each gene is represented by a node of a network, and each node has one of two states: on – i.e., producing (‘expressing’) its target protein – or off. Directed links between genes indicate that one gene influences the expression of another. This can correspond to the expressed protein directly binding to DNA and modulating the transcription of a gene or to other signaling pathways that modulate DNA transcription. In the standard Boolean network model, the system evolves in discrete timesteps ($t = 0, 1, 2, \dots$), and at each step the state of every node is simultaneously updated according to some function of its inputs. This function approximates the action of activators (proteins which act to increase expression of a given gene) or inhibitors (proteins which act to reduce expression). While this model might seem to be an oversimplification considering the complex kinetics involved in all steps of a transcription pathway, experimental evidence suggests that real biological systems are, in some cases, reasonably well-approximated by Boolean networks [41].

In 1969, S.A. Kauffman [39] introduced a type of Boolean network known as an N - K network. In this model, there are N nodes each having exactly K input

links, and the nodes from which these input links originate are chosen randomly with uniform probability. (K is not necessarily small compared to N .) We refer to the number of input (output) links to (from) a node as the in-degree (out-degree) of that node. At any given time t , the system state can be represented as an N -vector whose i th component $\sigma_i(t)$ is either zero or one, where $i = 1, 2, \dots, N$. There are 2^N possible states. The function determining the time evolution at each node is defined by a random, time-independent, 2^K -entry truth table. Since this is a finite, deterministic system, there is always an attractor: eventually, the system must return to a previously visited state (finiteness), after which the subsequent dynamics will be the same as for the previous visit (determinism). These attractors can be fixed points or periodic orbits. Using the Hamming distance between two states (i.e., the number of nodes for which the $\sigma_i(t)$ disagree) as the distance measure, the system exhibits both what is termed a ‘chaotic’ (or unstable) regime, where the distance between typical initially close states on average grows exponentially in time, as well as a stable regime, where the distance decreases exponentially. Between the two there is a ‘critical’ regime. (Here by ‘close’ we mean that the Hamming distance is small compared to N .)

As a model of genetic control, these attractors have been postulated to represent a specific pattern of protein expression which defines the cell’s character [39]. In single-celled organisms, these attractors might be taken to correspond to different cell states (growing, dividing, starving, heat- or pH-shocked). In multi-cellular organisms, different cell types (muscle, nerve, liver, etc.) have different expression patterns, and, within each type, a cell could be in a variety of states (resting, ‘acti-

vated,' dividing, etc.) that each correspond to different expression patterns. Boolean network approximations have been successful in predicting the gene expression time sequence of the segment polarity gene network in *Drosophila*, a model for embryonic development where individual cells turn specific proteins on and off in patterns that guide the growth of certain organs and structures [41]. Since the protein expression pattern of the cell is modeled from the state of the corresponding Boolean network, the question of the stability of the network then becomes important: do small perturbations in the expression pattern, due perhaps to chemical fluctuations, die out quickly, returning the cell to its original state, or do they quickly grow, pushing the cell into another state? The purpose of this paper is to examine the stability of network dynamics in the context of discrete state models of gene networks.

One motivation for the consideration of dynamical stability is its possible relevance to cancer. Specifically, we hypothesize that dynamical instability of a gene network might be a causal mechanism contributing to the occurrence of some cancers. We emphasize that this hypothesis is distinct from the previous hypothesis of 'genomic instability' as a cause of cancer [42]. In particular, genomic instability has been defined¹ as 'the failure to transmit an accurate copy of the entire genome from one cell to its two daughter cells.' In contrast, the instability we refer to is that of the *dynamics* of a *given* gene network, and we use the term 'dynamical network instability' (DNI) to distinguish this condition. We speculate that DNI might arise from mutations and that, once established, as cells divide, DNI could lead to widely varying gene expression patterns from cell to cell. We emphasize that DNI implies

¹As defined in the glossary of *Nature Genetics*

that this variation would arise even in the absence of further mutation. That is, similar to the concept of chaos in continuous-state dynamical systems (e.g., [43]), DNI causes exponential sensitivity of typical system trajectories to small changes, which we speculate may lead to many different outcomes in the course of cell division. Recent microdissection results indicate wide variations in gene expression patterns even for nearby cells within the same cancerous tissue [44]. This variability provides a basis for understanding why cancer can adapt and evade treatment [45].

Another motivation for our study is the argument, put forward by Kauffman [40], that evolution favors gene networks that are on the border between stability and instability [46, 47, 48, 49]. Whether or not our cancer hypothesis or Kauffman’s stability-border hypothesis holds, the question of dynamical stability of such networks is crucial to their understanding and use as models.

While previous works have addressed the question of dynamical network stability in simple, specific types of random networks (e.g. $N - K$ nets), in this paper we address the question of dynamical network stability for general network topology and node attributes. We also consider nonsynchronous update and extend the considerations to non-Boolean models allowing for the possibility of nodes having more than two states. Thus our work provides a potentially enhanced framework for modeling and using the discrete state network paradigm. In particular, we consider how our network stability considerations can be employed on experimentally derived gene networks.

In the original $N - K$ nets as proposed by Kauffman, the truth table output governing node dynamics was randomly chosen with on and off having equal prob-

ability. Subsequently, it was shown that if the truth table output was biased such that p denotes the probability of randomly assigning an off output, the transition between the stable and chaotic regimes depends on p [50]. We term p the ‘expression bias.’ Additionally, networks with a distribution of in-degrees, but no in-/out-degree correlation, have been considered in [51, 52, 53, 54], and it has been shown that the nodal in-degree average, $\langle K^{in} \rangle$, suffices to determine the stability. (Here $\langle \cdot \rangle$ indicates average of a nodal quantity over all nodes.) Specifically, the critical average number of connections, K_c , governing this transition is

$$K_c = 1/[2p(1 - p)], \quad (3.1)$$

where the network is stable for $\langle K^{in} \rangle < K_c$, unstable for $\langle K^{in} \rangle > K_c$, and critical for $\langle K^{in} \rangle = K_c$. Aldana and Cluzel [54] considered the consequences of Eq. (3.1) in the case of networks with scale-free topology [55], i.e., the probability distribution $P(K^{in})$ (or $P(K^{out})$) that a randomly chosen node has in-degree K^{in} (out-degree K^{out}) is a power-law: $P(K) \propto K^{-\gamma}$. (Since every out-link for a node is an in-link for some other node, $\langle K^{in} \rangle = \langle K^{out} \rangle$; thus the result is unchanged whether it is the in- or out-degree that has power-law scaling.) In the case of power-law distributions, Eq. (3.1) can be rewritten in terms of γ , and there is a rather large range of γ where the network is stable.

Recently, some authors have noted, but not numerically tested, a generalization of Eq. (3.1) that takes into account nodal correlations between the in-degree and out-degree characterized by the joint $K^{in} - K^{out}$ degree distribution function

$\tilde{P}(K^{in}, K^{out})$. In this case, the critical transition occurs at [65]

$$\frac{\langle K^{in} K^{out} \rangle}{\langle K \rangle} = \frac{1}{2p(1-p)}. \quad (3.2)$$

We emphasize that Eq. (3.1) was derived in the annealed approximation (see later discussion) for networks with a given in- or out-degree distribution $P(K)$ and with the complimentary links completely random, and that Eq. (3.2) uses only the additional information contained in the nodal in-/out-degree correlation. Furthermore, all nodes (‘genes’) were taken to have the same p value. However, gene networks, in common with real networks occurring across a broad range of applications, can be expected to deviate substantially from the above simple network model. Examples of network properties that could make previous analyses of network stability inapplicable are assortativity [56] (the tendency for highly connected nodes to prefer or avoid linking to other highly connected nodes) and community structure [57] (the existence of highly connected, sparsely interconnected subgraphs), two properties that are not captured in the degree distributions. Additionally, these properties may have biological implications. For example, a recent paper [58] examined gene interaction networks from cancerous tissue and found significant community structure, as well as positive correlation between the in-degree and out-degree of nodes; additionally, protein interaction networks have been shown to exhibit significant disassortativity [56, 59]. Furthermore, for modeling purposes, it might be important to allow the expression bias p to vary from node to node (as an extreme example, so-called housekeeping genes [60] have a predominant tendency to be on, corresponding to low p , unlike other genes). In this paper, we derive and test the stability criterion

for large networks with arbitrary network topology and heterogeneous expression biases. In particular, our theory evaluates the stability of any given network with its specific topology (i.e., its adjacency matrix A defined subsequently), and by its node-specific expression biases. We show that stability is determined by the largest eigenvalue of a modified adjacency matrix, and we numerically test this criterion.

With respect to real gene networks, the synchronous update at integer times ($t = 0, 1, 2, \dots$) used in the above models represents an additional deviation from the real situation, where chemical kinetics and transport processes can be expected to introduce non-trivial dynamics. As a partial step toward remedying this (and to make Boolean approximations suitable for atmospheric and geophysical processes), Ghil and Mullhaupt [61] consider a generalization in which t is a continuous variable and $\sigma_i(t)$ depends on $\sigma_j(t - \tau_{ij})$, where τ_{ij} is a delay time that can be different for each link from j to i . The original formulation (e.g., in Refs. [39, 50, 51, 52, 53, 54]) corresponds to $\tau_{ij} = 1$ for all i, j . We will argue and numerically confirm that the criterion determining the stability/instability border of this generalization of the Boolean network model is the same as that for the synchronous update models.

In addition to nonsynchronous update, another generalization of Boolean networks that we will examine is models in which each node i is allowed to have one of S_i possible discrete states (e.g., for $S_i = 3$, we label the states $\sigma_i \in \{0, 1, 2\}$, and for Boolean networks $S_i = 2$ for all i). This model may be closer to the behavior of actual cells, and models with multiple states can be related to certain piece-wise ODE models of transcription [62, 63]. The general model using arbitrary, multivalued truth tables has been previously treated in the special case of $N - K$ networks

with all nodes having the same number of possible states S . In the case where each possible state is equally likely, the critical number of inputs is ²

$$K_c = \frac{1}{1 - 1/S}. \quad (3.3)$$

The applicability of our work to any specific network and set of node-wise expression biases may be of particular interest in situations where experimental data provide the possibility of estimating a gene network and expression biases. Such information could be used as input to our method which could give an indication of the stability of a given experimentally-derived network. The possibility that such analyses may be feasible becomes more and more likely with the rapid technological advances in obtaining new types of high-quality, quantitative data useful for deducing gene networks. For example, such analyses could be used to address the hypothesis that dynamical instability of gene networks is connected with the occurrence of cancer.

3.2 Model

Deterministic Boolean networks are formally defined by a state vector $\Sigma(t) = [\sigma_1(t)\sigma_2(t)\dots\sigma_N(t)]^T$, where $\sigma_i \in \{0, 1\}$, and a set of update functions f_i , such that

$$\sigma_i(t) = f_i(\sigma_{k(i,1)}(t-1), \sigma_{k(i,2)}(t-1), \dots), \quad (3.4)$$

where $k(i, 1), k(i, 2), \dots, k(i, K_i^{in})$ denote the indices of the K_i^{in} nodes that input to node i ; we denote this set of nodes by $\mathcal{K}_i = \{k(i, j) | j = 1, 2, \dots, K_i^{in}\}$. The update

²Unpublished results by Sole, RV, Luque, B, and Kauffman, S.

function f_i is defined at each node i by specifying a truth table whose outputs are randomly populated. Previous analytic results assumed a constant expression bias for all nodes; however, we allow that, in the truth table for node i , output entries are randomly assigned zero with probability p_i or one with probability $1 - p_i$. In the case of uniform expression bias, we drop the subscript and use the notation $p \equiv p_i$.

We consider the interaction structure of this system as a graph where the nodes represent individual elements of the state vector, and a directed edge is drawn from node j to node i if $j \in \mathcal{K}_i$. An adjacency matrix A is defined in the usual way: a matrix entry A_{ij} is one if there is a directed edge from node j to node i and zero otherwise.

The stability of a large Boolean network is defined by considering the trajectories resulting from two close initial states, $\Sigma(t)$ and $\tilde{\Sigma}(t)$. To quantify their divergence, the Hamming distance of coding theory is used: $h(t) = \sum_{i=1}^N |\sigma_i(t) - \tilde{\sigma}_i(t)|$. If the network is stable, on average $h(t) \rightarrow 0$ as $t \rightarrow \infty$. In unstable networks, $h(t)$ quickly increases to $O(N)$, while a ‘critical’ network is at the border separating stability and chaos.

In order to study the stability of an $N - K$ Boolean network, Derrida and Pomeau [50] considered an annealed situation and calculated the probability that, after t steps, a node state is the same on two trajectories that originated from initially close conditions. (This calculation was later generalized to variable in-degree [51, 52, 53], and joint degree distribution in [65].) In Derrida and Pomeau’s ‘annealed’ situation, at *each* time step t the truth table outputs and the network of connections are randomly chosen. The actual situation of interest, however, is

the case of ‘frozen-in’ networks, where the truth table and network of connections are fixed in time. It has been commonly assumed that analytical results obtained for the annealed case are a good approximation to the frozen-in case (e.g., Refs. [50, 51, 52, 53]). We also adopt this view in a modified form, and we will test its predictions with numerical simulations.

The randomization of the network of connections at each time step while keeping the degree distribution fixed carries the implicit assumption that there is no additional dynamically relevant structure in the frozen network other than that contained in the joint degree-distribution $\tilde{P}(K^{in}, K^{out})$. To avoid this assumption, we obtain theoretical results for a different annealing protocol, which we term ‘semi-annealed.’ In this semi-annealed procedure, we keep the network fixed (i.e., the adjacency matrix A does not change with time), and we envision randomly assigning the output entries of the truth table of each node i at every time t according to the time-independent expression bias p_i assigned to node i . We then imagine tracking the probability that individual node states $\sigma_i(t)$ and $\tilde{\sigma}_i(t)$ differ over time with an N -dimensional difference vector, whose components are $y_i(t) = \langle\langle |\sigma_i(t) - \tilde{\sigma}_i(t)| \rangle\rangle$, where $\langle\langle \cdot \rangle\rangle$ denotes an average over every possible small initial perturbation. Here by ‘every possible small initial perturbation’ we mean all perturbations for which a small fraction ϵ of the states are flipped. Additionally, we define the ‘sensitivity’ q_i as the probability that the output of f_i changes when given two different input strings, similar to the ‘average sensitivity’ of Ref. [64]. In the case of completely

random Boolean functions,

$$q_i = 1 - \left(p_i^2 + (1 - p_i)^2 \right) = 2p_i(1 - p_i). \quad (3.5)$$

Thus, similar to Ref. [50], we can write the update equation for y_i as

$$y_i(t) = q_i \left(1 - \prod_{j \in \mathcal{K}_i} (1 - y_j(t-1)) \right). \quad (3.6)$$

Equation (3.6) follows from noting that the probability that σ_j and $\tilde{\sigma}_j$ are equal is $(1 - y_j)$ and thus the probability that all inputs to node i are equal is the above product. Note that this equation uses topological information contained in the \mathcal{K}_i . However, we have treated y_j , $y_{j'}$ and q_i as if they were probabilities of statistically independent random events. We hypothesize that this semi-annealed protocol might be expected to yield good results for frozen-in cases when the network is large and the fraction of network nodes on short loops is small (the network is ‘locally tree-like’). To see the problem posed by short loops, consider a node with two inputs that themselves have inputs both coming from a common node; in this case, the elements of $y(t)$ in Eq. (3.6) are no longer statistically independent and multiplying the probabilities is no longer correct. See Ref. [66] for discussion related to the locally tree-like assumption. Our numerical tests of frozen networks indeed yield results that agree very well with our semi-annealed hypothesis on large, locally tree-like networks. We also find our predictions to hold for networks with a large number of feedforward motifs, a nontree-like three-node subgraph that has been found to be prevalent in real gene networks [67].

The case where both network states are exactly the same corresponds to $y_i(t) = 0$, which is a fixed point of Eq. (3.6). In order to determine the stability of this

fixed point, we linearize Eq. (3.6) around $y(t) = 0$ for small perturbations:

$$y_i(t+1) \approx q_i \sum_{j=1}^N A_{ij} y_j, \quad (3.7)$$

where A_{ij} are the elements of the adjacency matrix A . Equation (3.7) can be written in matrix form as $y(t+1) = Qy(t)$ where

$$Q_{ij} = q_i A_{ij}. \quad (3.8)$$

The stability is thus governed by the largest eigenvalue λ_Q of this matrix:

$$\begin{aligned} \lambda_Q > 1, y = 0 \text{ is unstable;} \\ \lambda_Q = 1, y = 0 \text{ is critical;} \\ \lambda_Q < 1, y = 0 \text{ is stable.} \end{aligned} \quad (3.9)$$

Since $Q_{ij} \geq 0$, the Perron-Frobenius theorem [68] guarantees that λ_Q is real and positive. We also note that, for any given adjacency matrix A and assignment of q_i 's to nodes, Eq. (3.6) can be iterated numerically to predict the expected time-asymptotic saturation value of the difference in two initially nearby states when evolved to steady-state. We numerically test this prediction, as well as the stability criterion in Eq. (3.9) in the next section. ³

As a special case of interest, if the the q_i are uniform, $q_i \equiv q$, then $\lambda_Q = q\lambda$, where λ is the maximum eigenvalue of the adjacency matrix. This yields the critical condition,

$$\lambda = 1/q. \quad (3.10)$$

³We note that Eq. (3.8) and the condition $\lambda_Q = 1$ also occurs in the treatment [66] of site percolation on directed networks where different sites have different removal properties. A similar condition involving $\langle K^2 \rangle / \langle K \rangle$ also arises in percolation on undirected networks [78].

Furthermore, for the case of a large network whose links are randomly assigned subject to a joint probability distribution $\tilde{P}(K^{in}, K^{out})$ at each node (with no assortativity), the mean field approximation for the largest eigenvalue is [69]

$$\lambda \approx \frac{\langle K^{in} K^{out} \rangle}{\langle K \rangle}, \quad (3.11)$$

where, since $\langle K^{in} \rangle = \langle K^{out} \rangle$ necessarily, we use the notation $\langle K \rangle \equiv \langle K^{in} \rangle = \langle K^{out} \rangle$. Equations (3.10) and (3.11) yield the same criterion as in Eq. (3.2). In the case where K^{in} and K^{out} are uncorrelated, $\tilde{P}(K^{in}, K^{out}) = P_{in}(K^{in})P_{out}(K^{out})$ and $\langle K^{in} K^{out} \rangle = \langle K \rangle^2$, yielding Eq. (3.1).

The eigenvalue of random network adjacency matrices with assortativity has been considered in Ref. [69], which defines an assortativity measure ρ as

$$\rho = \frac{\langle K_i^{in} K_j^{out} \rangle_e}{\langle K^{in} K^{out} \rangle}, \quad (3.12)$$

where $\langle K_i^{in} K_j^{out} \rangle_e$ denotes an average over all links (i, j) from node i to node j . The network is assortative (disassortative) if $\rho > 1$ ($\rho < 1$). For ρ near one, the largest eigenvalue λ is approximately given by [69]

$$\lambda \approx \frac{\langle K^{in} K^{out} \rangle}{\langle K \rangle} \rho. \quad (3.13)$$

Thus by Eqs. (3.6) and (3.9), it is predicted that, for uniform q , assortativity (disassortativity) decreases (increases) the critical q value.

In the case of nonuniform q_i , we have recently generalized Eq. (3.11) to obtain an analogous mean field approximation to λ_Q without assortativity or community structure,

$$\lambda_Q \approx \frac{\langle q K^{in} K^{out} \rangle}{\langle K \rangle}. \quad (3.14)$$

Our derivation of (3.14) will be published elsewhere. From (3.14), we see that correlation (anticorrelation) between q and $K^{in}K^{out}$ decreases (increases) network stability and that, in the absence of correlation, the result is similar to that for a uniform q , $\lambda_Q \approx \langle q \rangle \langle K^{in}K^{out} \rangle / \langle K \rangle$, with $\langle q \rangle$ replacing the uniform q (Eqs. (3.9) and (3.10)).

We now consider the generalization to allow any number of discrete node states. We denote the number of possible states of node i by S_i , and we label the possible states $0, 1, 2, \dots, S_i - 1$. The number of possible inputs to i from the set \mathcal{K}_i of nodes that influence it is $\prod_{j \in \mathcal{K}_i} S_j$. For each of these possible inputs, the truth-table function f_i in Eq. (3.4) assigns one of the S_i possible states to node i . Similar to the Boolean case, we take the assignment to be random and to have an ‘expression bias’ $p_{i,s}$ for each of the $s = 0, 1, 2, \dots, S_i - 1$ node states, where $p_{i,s}$ denotes the probability that f_i , for a given set of inputs, assigns the state s to node i , and $\sum_s p_{i,s} = 1$ for all nodes i . As in the Boolean case, we can then introduce the sensitivity q_i giving the probability that two different sets of inputs result in a different updated state of node i , which, in the random truth table case,

$$q_i = 1 - \sum_s p_{i,s}^2. \quad (3.15)$$

With this definition, we see that all our previous reasoning still applies, and Eqs. (3.6)-(3.9) hold with this generalized expression for the node sensitivities and with $y_i(t)$ interpreted as the probability of disagreement between $\sigma_i(t)$ and $\tilde{\sigma}_i(t)$. In the case of uniform number of node states $S_i \equiv S$ and equal expression biases $p_{i,s} \equiv p_s = 1/S$, among these states, Eq. (3.15) becomes $q = 1 - 1/S$, which, when

combined with Eq. (3.10) yields the previous result in Eq. (3.3).

Finally, we note that our criticality criterion, $\lambda_Q = 1$, is unchanged by the presence of delays, as in the models of Refs. [61], and only a slight modification is required of Eq. (3.6) (i.e., $y_j(t - \tau_{ij})$ replaces $y_j(t - 1)$). The condition $\lambda_Q = 1$ implies that the components of y in Eq. (3.6) are time-independent. Thus we predict that the delays τ_{ij} do not influence the result, and the criticality condition in Eq. (3.9) is independent of the synchronous update structure of the most commonly used random Boolean network models. Similarly, the time-asymptotic steady state obtained by repeated iteration of (3.6) is, by definition, time-independent and thus also does not depend on the τ_{ij} (although the τ_{ij} will influence the time-dependent approach to the asymptotic steady state; see Appendix C).

3.3 Statistical Methods

We numerically test the above predictions on several classes of Boolean networks with uniform sensitivity (i.e., $q_i = q$ is the same for all nodes):

- (a) random networks with $K^{in} = K^{out}$;
- (b) random networks with imperfect correlation between K^{in} and K^{out} ;
- (c) networks with assortativity or disassortativity; and
- (d) networks constructed as in (a) but with a substantial number of feedforward loops.

We additionally test our predictions on two classes of networks with nonuniform sensitivities:

- (e) networks constructed as in (a) but where nodes have different sensitivities correlated with the degrees of the nodes; and
- (f) networks with significant community structure, where the two communities have different, uniform sensitivities.

Finally, we test our generalization to more than two node states on networks of type (a) but with $S_i = 4$ for all nodes. For types (a)-(c) and (e), we use networks with truncated power-law degree distributions. (Evidence for the presence of this type of distribution in gene networks has been seen in [70].)

The algorithms for constructing the networks of types (a)-(c) are as follows. (i) Establish the in- and out-degrees for each node, which are drawn from a distribution,

$$P(K) \propto \begin{cases} K^{-\gamma}, K \leq K^{max}, \\ 0, K > K^{max}, \end{cases} \quad (3.16)$$

where $\gamma = 2.1$ and $K^{max} = 15$ (Boolean case) or $K^{max} = 8$ ($S_i = 4$ case). The out-degree is initially set to the in-degree. (ii) Randomly swap the out-degrees between pairs of nodes. If maximal correlation between in- and out-degrees is desired, as in (a), this step is skipped so that $K^{in} = K^{out}$ and $\langle K^{in} K^{out} \rangle$ is maximal. A completely uncorrelated network has every nodal out-degree swapped exactly once, yielding $\langle K^{in} K^{out} \rangle = \langle K \rangle^2$. The quantity $\langle K^{in} K^{out} \rangle$, which approximately determines λ by Eq. (3.11), can thus be tuned by the number of nodes that have their out-degrees

swapped. (iii) Place links randomly between nodes subject to the constraints of the specified in- and out-degrees assigned at each node by the ‘configuration model’ [71]. (iv) If networks with assortativity (disassortativity) are desired, as in (c), perform a given number of link swaps, as in [69], that increase (decrease) the assortativity ρ in Eq. (3.12). In all cases we employ networks with $N = 10^4$ and two initial conditions separated by a Hamming distance of 100. In Appendix C we discuss finite size effects that can occur for smaller N .

We emphasize that, although we determine our networks randomly, in our numerical experiments we do not average over this randomness. Rather, we generate one random network for each experiment and examine the resulting behavior of that specific network.

3.4 Results

We test the steady-state predictions of Eq. (3.6) and the criticality condition of Eq. (3.9) in Fig. 3.1, and compare the calculated critical parameters to the mean-field-type approximations of Eqs. (3.11), (3.12), and (3.14) in Appendix C. In order to compare Eq. (3.6) (solid curves in Fig. 3.1) to experimental measurements of the Hamming distance from numerical evolution of true frozen Boolean dynamical systems (markers in Fig. 3.1), we calculate the node averaged steady-state fractional Hamming distance,

$$\bar{y} = \lim_{t \rightarrow \infty} \frac{1}{N} \sum_i y_i(t). \quad (3.17)$$

In practice, this limit is calculated as the average Hamming distance from $t = 90$ to $t = 100$ when all delays are the same ($\tau_{ij} = 1$), and from $t = 490$ to $t = 500$ when nonuniform delays are present. These times are well after the steady-state value is reached (see Appendix C). Each experimental data point in Fig. 3.1 corresponds to a single realization of interconnections averaged over 100 realizations of the time-independent truth table with specified sensitivity as before.

3.4.1 In-/Out-degree Correlations and Heterogeneous Time Delay

Figure 3.1(a) shows the steady-state Hamming distance as a function of the sensitivity for one network of type (a) ($\lambda = 4.4$) and two of type (b) ($\lambda = 2.9, 2.3$). The closed markers in the figure represent experiments with uniform delay $\tau_{ij} = 1$ on all links, while the open markers correspond to experiments where half the links, randomly chosen, have $\tau_{ij} = 10$ and the remainder have $\tau_{ij} = 1$. Importantly, the degree distributions are the same for all three networks, and we attain different λ values by varying the correlation between the in-degree and the out-degrees. We see from Fig. 3.1(a) that there is close agreement between the theoretical prediction and the experimental results and our prediction that the presence of delays does not change the stability is confirmed. Additionally, the measured steady-state Hamming distance is essentially zero below the critical value of the sensitivity, $q_{crit} = 1/\lambda$ (this point is indicated by vertical downward arrows in Fig. 3.1(a)). We emphasize that the degree distributions (and hence $\langle K \rangle$) are the same for the networks in Fig. 3.1(a), and thus, if the in-/out-degree correlation were ignored, the observed

difference between the stability conditions for these networks would not be predicted.

3.4.2 Assortativity/Disassortativity

Figure 3.1(b) shows results obtained when significant assortativity or disassortativity is present (type (c) networks). In this experiment, as well as all those reported below, the delays are all uniform. The networks under consideration have the same joint degree-distribution with $K^{in} = K^{out}$. However, each of the networks have very different assortativities ($\rho = 0.52, 1.0, 1.7$, defined in Eq. (3.12)), which yield different largest eigenvalues ($\lambda = 3.0, 4.4, 9.9$). Since the joint degree distributions are the same, Eq. (3.2) would predict that the three networks have the same stability characteristics. However, since their eigenvalues are very different, we predict that, as observed, the transitions of the three networks occur at different values of q . Again the theoretical predictions of q_{crit} are indicated by vertical arrows.

3.4.3 Motifs

Random construction of networks, as used in the networks above, is expected to yield networks that are locally tree-like [69]. However, we note that biological and other types of networks often have motifs (small subgraphs) that occur with higher frequency than in randomly constructed networks [67]. For gene networks of *E. coli* and *S. cerevisiae*, it was found that the number of feedforward loop motifs (see inset to Fig. 3.1(c)) is significantly enhanced compared to the expected number in a randomly constructed network. In these networks, the number of feedforward

loops per node c is roughly 0.1. Thus we consider a network of type (a) ($\lambda \approx 2.9$ and $N = 10^4$) after adding 1000 ($c = 0.1$) and, in an extreme case, 2000 ($c = 0.2$) feedforward loops. To add a feedforward loop, we randomly choose a node A , follow a random output to node B , and follow a random output of B to node C . We then add a link from node A to node C . We do this a given number of times, avoiding nodes that already participate in an added feedforward loop. In Fig. 3.1(c), we see that the semi-annealed theory of Eq. (3.6) (solid curve) again agrees well with our numerical experiments (solid markers). Based on such results, we believe that the locally tree-like network requirement does not invalidate application of our method to real gene networks. We also note that the critical point is essentially unchanged by the addition of loops (adding links only slightly increases the largest eigenvalue), however more feedforward loops tend to increase the steady-state Hamming distance for $q > q_{crit}$.

3.4.4 Application to *S. cerevisiae*

As a real biological example, we include in Appendix C a graph similar to those in Figs. 3.1(a)-(c) using a published network for the yeast *S. cerevisiae* [79].

3.4.5 Heterogeneous Correlated Sensitivities

Figure 3.1(d) demonstrates the effect of a distribution of q_i 's on the stability of a network with $K_i^{in} = K_i^{out} = K_i$ and with correlation between the nodal values of q_i and K_i , i.e., type (d) networks. We consider two situations, one where

$\langle qK^2 \rangle / (\langle q \rangle \langle K^2 \rangle)$ is maximal, and one where it is minimal. The q_i are drawn from a uniform distribution centered at q_0 (the abscissa in the figure), with width $\Delta q = 0.1$. Maximal (minimal) $\langle qK^2 \rangle$ is attained by assigning the largest q_i to the node with the largest (smallest) K_i , the second largest q_i to the node with the second largest (second smallest) K_i , and so on. As can be seen from the figure, there is good agreement between the semi-annealed theory and the numerical experiments, and the two networks become unstable at different values of q_0 . (Vertical arrows again indicate the points where $\lambda_Q = 1$.)

3.4.6 Community Structure

Figure 3.1(e) shows our results for a case where there is community structure and community-dependent sensitivity. To construct the networks in Fig. 3.1(e), consider the case where there are two communities, and we assign a link from node i in community a to node j in community b with probability θ_{ab} . We impose the additional constraints that $\theta_{aa} = \theta_{bb} \equiv \theta_U$ and that $\theta_{ab} = \theta_{ba} \equiv \theta_\cap$, and the size of the two communities are the same, $N/2$. We take $\langle K^{in} \rangle = \langle K^{out} \rangle = \langle K \rangle = (\theta_U + \theta_\cap)N$ to be the same for both communities, and we also assume that communities a and b have different sensitivities q_a and q_b , respectively. As θ_\cap is increased from zero to $\theta_\cap = \theta_U$, λ_Q changes from the case of two completely separated communities to one of a single random network. Communities a and b have equal sizes of 5000 nodes, community a has $q_a = 0.5$, and community b has $q_b = 0.1$. In order to vary λ_Q , we vary θ_U and θ_\cap , keeping their sum constant in order to maintain constant $\langle K \rangle$.

As with the curves in Fig. 3.1(a)-(c), the transition to chaos is governed by λ_Q ($\lambda_Q = 1$ at the vertical arrow), and Eq. (3.6) (solid curve) accurately predicts the numerically observed (solid circles) steady-state Hamming distance.

3.4.7 Non-Boolean Models

Figure 3.1(f) illustrates an application to a case in which there are more than two possible states at each node. In particular, we consider $S \equiv S_i = 4$ possible states at each node. (Since the number of possible inputs to the truth table for node i in this case is $4^{K_i^{in}}$, we take $K^{max} = 8$ due to memory constraints.) Labeling the possible node states $\sigma_i \in \{0, 1, 2, 3\}$, we take nodes to have uniform expression biases for occurrence of state-label 0, $p_0 \equiv p_{i,0}$, from 0 to 1. The three remaining labels ($\sigma = 1, 2, 3$) also have uniform biases for all nodes i , $p_s \equiv p_{i,s} = (1 - p_{i,0})/3$. From Eq. (3.15), $q \equiv q_i = 1 - [p_0^2 + (1 - p_0)^2/3]$, which has a maximum $q_{max} = 0.75$ at $p_0 = 0.25$. As can be seen in the figure, the predicted fraction of nodes with differing states \bar{y} (solid curve) also has a maximum there. It is again seen that the measurements (markers) are well-predicted by the theory.

3.5 Discussion

In this paper, we have presented theoretical results (Eqs. (3.6) and (3.9)) which predict the steady-state Hamming distance between states evolved from two nearby initial conditions and the stability of a given network. These results are derived using the hypothesis that a theory derived in the semi-annealed case approximates

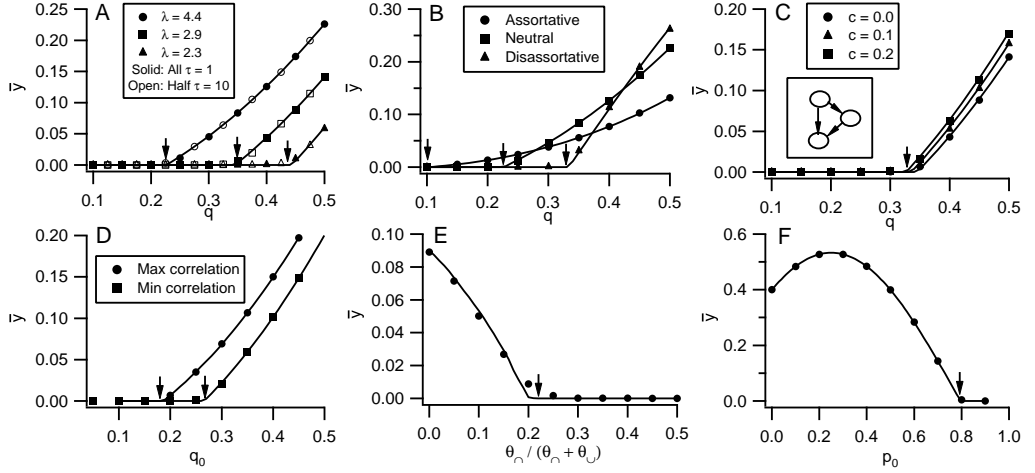


Figure 3.1: (a) \bar{y} vs. q for three networks with different largest eigenvalues ($\lambda \approx 5.5, 3.4, 2.3$), both with uniform delay on all links $\tau_{ij} = 1$ (closed markers) and with half the links having increased delay of $\tau_{ij} = 10$ (open markers). The solid curves correspond to the prediction \bar{y} (defined in Eq. (3.17)) obtained by simulating Eq. (3.6). The downward vertical arrows correspond to $q_{crit} = 1/\lambda$ for each of the three networks. (b) \bar{y} vs. q for three networks with different assortativities. (c) \bar{y} vs. q for networks with added feedforward motifs, with an illustration of the feedforward motif (inset). (d) \bar{y} vs. q_0 for networks with maximum correlation (circles) and minimum correlation (squares) between $K_i^{in} K_i^{out}$ and q_i , where q_i is drawn from a uniform distribution centered at q_0 with width 0.1. (e) \bar{y} vs. $\theta_\cap / (\theta_\cap + \theta_\cup)$ for networks with community structure, where the two communities have $q_a = 0.5$ and $q_b = 0.1$. (f) \bar{y} vs. p_0 for a network where each node can take one of $S_i = 4$ possible states. p_0 is the probability that a zero appears in the truth table output; the remaining three symbols appear with equal probability.

the true situation, where by semi-annealed we mean that the network of connections is frozen, but the truth table at each node is randomly reassigned at each timestep. For large networks, this approximation was found to give excellent agreement with the true case of frozen connections and frozen truth tables. Our semi-annealed hypothesis does not rely on gross statistical properties of the network, but instead uses the specific network topology, as characterized by the network adjacency matrix, and the individual node sensitivities to make predictions.

We tested our theoretical predictions with numerical experiments. Previously unaddressed issues that we considered include the effects of assortativity, nonuniform time delay, nonuniform sensitivity, motifs, and community structure. In all cases tested we found good agreement with our theory.

The theory that we have presented and tested above may represent a step forward in facilitating the application of discrete state dynamical network models to biological systems. Given a specific genetic interaction network and an estimate of the node sensitivities, Eq. (3.9) predicts the stability of that particular network directly from the adjacency matrix. Curated networks already exist in the literature for model single-cellular systems, and new algorithms continue to be developed for inferring interaction networks from a wide range of data sources (microarray experiments, GO annotation, genome sequencing, etc.). We note that such a procedure has the advantage that, because the actual experimentally determined network is employed, topological aspects such as nodal in-/out- degree correlation, assortativity, community structure, etc., do not first have to be determined and then statistically modeled. Thus, by use of our stability criterion (3.9), there is the potential that

future analysis may be able to evaluate a supposed relationship between the stability characteristics of various networks and their functioning. For example, one might test whether cancer gene networks are less stable than those in healthy tissue. This could lead to the strong variations in gene expression observed in cancerous tissue [44], even when the underlying gene network is unchanged. We are currently pursuing research along this line.

Chapter 4

Approximating λ_Q

4.1 Introduction

Topological properties of networks have received much attention. The coarsest topological property is the degree distribution, where the in-degree d_i^{in} and out-degree d_i^{out} of a network node i are defined as the number of directed network links pointing into and away from node i . At each node, the in-degree and out-degree may be correlated; this correlation can be characterized by

$$\eta = \langle d^{in} d^{out} \rangle / \langle d \rangle^2, \quad (4.1)$$

where $\langle \cdot \rangle$ denotes the average of the indicated quantity over all network nodes. (Since every out-link of a node is an in-link for some other node, $\langle d^{in} \rangle = \langle d^{out} \rangle \equiv \langle d \rangle$.) Additionally, networks can be assortative or disassortative [56], i.e., nodes with high degree may prefer or avoid connecting to other nodes of high degree. We characterize this by a correlation coefficient ρ between the in-degrees d_j^{in} and the out-degrees d_i^{out} at either end of a directed link from node j to node i [69]¹,

$$\rho = \langle d_i^{in} d_j^{out} \rangle_e / (\eta \langle d \rangle)^2, \quad (4.2)$$

¹This definition of ρ appears in Ref. [69]. Newman [56] characterizes assortativity using a different quantity, but Eq. (4.2) is more relevant for our purposes.

where $\langle \cdot \rangle_e$ indicates an average over all network links. If $\rho > 1$, the network is assortative, if $\rho < 1$ it is disassortative, and it is neutral if ρ is exactly one. Another example of topological structure is the existence of communities [81], which are groups of nodes that tend to be densely interconnected within the group but sparsely connected between groups.

In addition to static topological properties of networks, another area of recent interest has been dynamical processes taking place on networks. Examples include synchronization of coupled identical dynamical systems (which may be chaotic) [82], the onset of coherence in the evolution of heterogeneous network-coupled dynamical systems (both oscillatory [83], as well as chaotic [84]), the onset of instability in discrete state models of gene networks [85], percolation on directed networks [66], and others. In several of these examples [84, 85, 66], an important determining quantity was shown to be the maximum eigenvalue of the adjacency matrix A , the elements of which are defined to be $A_{ij} = 1$ if there is a directed link to node i from node j and zero otherwise for all $i, j = 1, 2, \dots, N$, where N is the number of network nodes; $A_{ii} \equiv 0$ by definition.

Motivated by the importance of λ_A to these dynamical problems, Ref. [69] developed theory for obtaining large N approximations to λ_A from knowledge of statistical characterizations of the network. For example, it was shown [69] that random networks constrained only by specification of the joint degree distribution $P(d^{in}, d^{out})$ have

$$\lambda_A \approx \langle d^{in} d^{out} \rangle / \langle d \rangle = \eta \langle d \rangle, \quad (4.3)$$

where $P(d^{in}, d^{out})$ is the probability that a randomly chosen node has in-degree d^{in} and out-degree d^{out} . From (4.3) it is seen that nodal correlation or anticorrelation between d^{in} and d^{out} increases or decreases λ_A . If an additional assortativity constraint is imposed, then Ref. [69] obtains

$$\lambda_A \approx \rho \eta \langle d \rangle, \quad (4.4)$$

to lowest order in $(\rho - 1)$. Thus assortativity ($\rho > 1$) tends to increase λ_A , and disassortativity ($\rho < 1$) tends to decrease λ_A .

However, we note that in two of the cited applications (namely, gene network stability [85] and site percolation on large directed networks [66]), the formulations resulted in a somewhat more general eigenvalue problem. Specifically, this problem was that of determining the largest eigenvalue λ_Q of a generalized adjacency matrix Q whose elements are given by

$$Q_{ij} = q_i A_{ij}, \quad (4.5)$$

where q_i is the ‘bias’ characterizing node i which may be different for each node. In the special case of uniform $q_i \equiv q$ for all i , the problem for λ_Q reduces to that for λ_A , i.e., $\lambda_Q = q\lambda_A$, and the previous results such as Eqs. (4.3) and (4.4) can be employed. However, it is also of interest to consider the more general problem of determining λ_Q for nonuniform biases, and it is that problem to which this paper is devoted. We note that in the site percolation context [66], $q_i = (1 - p_i)$, where p_i is the probability that node i is removed, while in the gene network context [85], q_i is the probability that the output of gene (node) i is switched to another state if one or more of its randomly chosen inputs is switched. In either case, q_i is in the

range $0 \leq q_i \leq 1$, and we accordingly restrict ourselves to $q_i \geq 0$. Since $Q_{ij} \geq 0$, the Frobenius-Perron theorem implies that λ_Q is real and positive.

Our analysis will consider ‘Markovian’ random networks (see Sec. 4.2). This type of consideration was used in the analysis of λ_A in Ref. [69], as well as in a variety of other interesting studies of different network related problems (e.g., Refs. [78, 86, 87, 88] which consider epidemic spreading and percolation). Basically, a Markovian network is one for which the only nontrivial spatial correlations are between nodes that are directly connected by a single link. Within this framework, we formulate a theory for determining the λ_Q of large networks, and we utilize our theory to examine several significant situations of interest. Examples of our results are a generalization of Eq. (4.3) (see Eq. (4.17)) showing that correlation between q and $d^{in}d^{out}$ increases λ_Q , a generalization of Eq. (4.4) (see Eq. (4.28)) showing that correlation between q_iq_j and $d_i^{out}d_j^{in}$ on edges from $j \rightarrow i$ increases λ_Q , and an analysis of the effect on λ_Q of network communities tending to have different, community-dependent q values (see Eq. 4.34).

For later reference we note the following relationships involving the adjacency matrix,

$$d_j^{in} = \sum_{i=1}^N A_{ij}, \quad d_i^{out} = \sum_{j=1}^N A_{ij}, \quad (4.6)$$

$$\langle S_{ij} \rangle_e = \left[\sum_{i,j} A_{ij} S_{ij} \right] / \sum_{i,j} A_{ij}. \quad (4.7)$$

By (4.6)

$$\langle d^{in} \rangle = \langle d^{out} \rangle = \frac{1}{N} \sum_{i,j} A_{ij} \equiv \langle d \rangle. \quad (4.8)$$

By (4.6)-(4.8)

$$\begin{aligned}\langle d_i^{out} \rangle_e &= \left[\sum_{i,j} A_{ij} d_i^{out} \right] / \sum_{i,j} A_{ij} = \sum_i d_i^{out} d_i^{in} / \sum_{i,j} A_{ij} \\ &= \langle d^{in} d^{out} \rangle / \langle d \rangle.\end{aligned}\tag{4.9}$$

4.2 Markovian Networks

We characterize each node i by four attributes: its in-degree d_i^{in} , its out-degree d_i^{out} , its ‘bias’ q_i , and its group (or community), labeled σ_i . We call the triplet $\underline{z}_i = (d_i^{in}, d_i^{out}, q_i)$ the ‘generalized degree’ of node i . The number of groups is denoted s , so that $\sigma = 1, 2, \dots, s$. If no two nodes have the same attributes (\underline{z}, σ) , then there is a one-to-one correspondence between i and $(\underline{z}, \sigma) \in \{(\underline{z}_k, \sigma_k) | k = 1, 2, \dots, N\}$. We consider N -node random networks specified by the following quantities: (i) the number of nodes in each group N_σ ($\sum_{\sigma=1}^s N_\sigma = N$); (ii) the degree distribution $P_\sigma(\underline{z})$ for group σ ($\sigma = 1, 2, \dots, s$) giving the probability that a node randomly chosen from group σ has generalized degree \underline{z} ; and (iii) the probability $\Pi(\underline{z}, \sigma | \underline{z}', \sigma')$ that, if a randomly chosen link originates from a node in group σ' that has degree \underline{z}' , then that link points to a node in group σ with degree \underline{z} . Note that, since every out-link for a node is an in-link for some other node, the degree distributions $P_\sigma(\underline{z})$ are constrained to satisfy the relation,

$$\sum_{\underline{z}, \sigma} N_\sigma P_\sigma(\underline{z}) d^{out} = \sum_{\underline{z}, \sigma} N_\sigma P_\sigma(\underline{z}) d^{in},\tag{4.10}$$

which we denote $N\langle d \rangle$. Furthermore, we have that $\Pi(\underline{z}, \sigma | \underline{z}', \sigma')$ satisfies the probability normalization condition,

$$\sum_{\underline{z}, \sigma} \Pi(\underline{z}, \sigma | \underline{z}', \sigma') = 1. \quad (4.11)$$

By use of this model, we essentially assume that the only non-trivial correlation between the attributes of two different nodes occurs when they are directly connected by a single link. For example, if we choose a random outward path of length two from a node in group σ_a of degree \underline{z}_a , then the probability that the first leg of the path goes to a node having $(\underline{z}_b, \sigma_b)$, and the second leg of the path goes to a node having $(\underline{z}_c, \sigma_c)$ is given by $\Pi(\underline{z}_c, \sigma_c | \underline{z}_b, \sigma_b) \Pi(\underline{z}_b, \sigma_b | \underline{z}_a, \sigma_a)$.

In order to find the maximum eigenvalue of Q , we consider the iteration $u^{(n+1)} = Qu^{(n)}$ which, for a typical initial choice of $u^{(0)}$ converges on the eigenvector u corresponding to the largest eigenvalue λ_Q . Relabeling the nodes by their attributes (\underline{z}, σ) , we write the components of the vector $u = [u_1, u_2, \dots, u_N]^T$ as $u_i = v(\underline{z}_i, \sigma_i)$. The ensemble average of the iterated vector $v^{(n)}(\underline{z}, \sigma)$ thus evolves according to

$$v^{(n)}(\underline{z}, \sigma) = q \sum_{\sigma'} \sum_{\underline{z}'} \Pi(\underline{z}, \sigma | \underline{z}', \sigma') (d^{out})' v^{(n)}(\underline{z}', \sigma'), \quad (4.12)$$

and we denote the eigenvalue of this evolution by $\hat{\lambda}_Q$,

$$\hat{\lambda}_Q v(\underline{z}, \sigma) = q \sum_{\sigma'} \sum_{\underline{z}'} \Pi(\underline{z}, \sigma | \underline{z}', \sigma') (d^{out})' v(\underline{z}', \sigma'). \quad (4.13)$$

For large N , and a random draw from our Markov ensemble of networks, we suppose that $\hat{\lambda}_Q$ from (4.13) will typically provide a good approximation to λ_Q for the chosen network, and we will test this supposition using numerical experiments.

In the next section, we apply Eq. (4.13) to obtain analytical approximations to λ_Q for several situations of interest.

4.3 Evaluation of λ_Q

4.3.1 The Effect of Nodal Correlations

We first consider the case $s = 1$, corresponding to the absence of group structure. Thus the variable σ may be omitted from Eq. (4.13). We furthermore assume that \underline{z}_i and \underline{z}_j on the two ends of a link from j to i are uncorrelated. Thus there is no assortativity, and $\Pi(\underline{z}|\underline{z}')$ does not depend on \underline{z}' . Under this assumption, $\Pi(\underline{z}|\underline{z}')$ is simply the probability that a randomly chosen link points toward a node with degree \underline{z} . This probability is proportional to the number of nodes with degree \underline{z} , and to the number of in-links to such a node,

$$\Pi(\underline{z}|\underline{z}') = d^{in} P(\underline{z}) / \langle d \rangle, \quad (4.14)$$

where the factor $\langle d \rangle^{-1}$ provides the necessary normalization from Eq. (4.11). Inserting (4.14) into (4.13) we have that

$$\hat{\lambda}_Q v(\underline{z}) = q d^{in} P(\underline{z}) \langle d \rangle^{-1} \sum_{\underline{z}'} (d^{out})' v(\underline{z}'). \quad (4.15)$$

Thus we see that the eigenvector $v(\underline{z})$ is

$$v(\underline{z}) = q d^{in} P(\underline{z}), \quad (4.16)$$

which when inserted into (4.15) yields

$$\hat{\lambda}_Q = \langle q d^{in} d^{out} \rangle / \langle d \rangle, \quad (4.17)$$

where

$$\langle qd^{in}d^{out} \rangle = \sum_{\underline{z}} qd^{in}d^{out}P(\underline{z}). \quad (4.18)$$

Equation (4.17) is the appropriate generalization of Eq. (4.3) to take into account the node-dependent biases q_i that appear in the definition, Eq. (4.5), of the matrix Q .

If q and $d^{in}d^{out}$ are uncorrelated, $\hat{\lambda}_Q = \langle q \rangle \hat{\lambda}_A$ where $\hat{\lambda}_A$ is given by (4.3). On the other hand, we see that if q and $d^{in}d^{out}$ are correlated (anticorrelated), then $\hat{\lambda}_Q$ is larger (smaller) than $\langle q \rangle \hat{\lambda}_A$.

4.3.2 Assortativity

Next we wish to consider how the result in Eq. (4.17) is modified if we allow correlation between \underline{z} and \underline{z}' . We address this problem perturbatively, and we write $\Pi(\underline{z}|\underline{z}')$ as

$$\Pi(\underline{z}|\underline{z}') \approx \Pi^{(0)}(\underline{z}|\underline{z}') + \epsilon\Pi^{(1)}(\underline{z}|\underline{z}'), \quad (4.19)$$

where ϵ is a small expansion parameter, and $\Pi^{(0)}(\underline{z}|\underline{z}')$ is given by the uncorrelated result, Eq. (4.14). Similarly expanding the eigenvalue $\hat{\lambda}_Q$ and the eigenvector $v(\underline{z})$, we have

$$\hat{\lambda}_Q \approx \hat{\lambda}_Q^{(0)} + \epsilon\hat{\lambda}_Q^{(1)}, \quad (4.20)$$

$$v(\underline{z}) \approx v^{(0)}(\underline{z}) + \epsilon v^{(1)}(\underline{z}), \quad (4.21)$$

where $\hat{\lambda}_Q^{(0)}$ is given by (4.17) and $v^{(0)}(\underline{z})$ is given by (4.16). Inserting (4.19)-(4.21), (4.14), (4.16), and (4.17) into (4.13), multiplying the resulting equation by d^{out} ,

and summing over all \underline{z} , the terms involving $v^{(1)}(\underline{z})$ cancel. Thus we obtain

$$\epsilon \hat{\lambda}_Q^{(1)} \hat{\lambda}_Q^{(0)} = \epsilon \sum_{\underline{z}, \underline{z}'} q d^{out} (d^{in})' q' \Pi^{(1)}(\underline{z} | \underline{z}') \tilde{P}(\underline{z}), \quad (4.22)$$

where

$$\tilde{P}(\underline{z}) = d^{out} P(\underline{z}) / \langle d \rangle. \quad (4.23)$$

is the probability that a randomly chosen link originates from a node of generalized degree \underline{z} . With this interpretation of (4.23), we see that (4.22) can be re-expressed in terms of the link average $\langle \cdot \rangle_e$,

$$\epsilon \hat{\lambda}_Q^{(1)} \hat{\lambda}_Q^{(0)} = \epsilon \langle q_i d_i^{out} d_j^{in} q_j \rangle_e - \langle q_i d_i^{out} \rangle_e \langle q_j d_j^{in} \rangle_e, \quad (4.24)$$

where we use the convention that j (i) labels the node that the link comes from (points to).

Proceeding as in Eq. (4.9), we obtain

$$\langle q_i d_i^{in} \rangle_e = \langle q_j d_j^{in} \rangle_e = \langle q d^{in} d^{out} \rangle / \langle d \rangle = \hat{\lambda}_Q^{(0)}, \quad (4.25)$$

which when inserted in (4.24) yields

$$\hat{\lambda}_Q \approx \hat{\lambda}_Q^{(0)} + \epsilon \hat{\lambda}_Q^{(1)} = \langle q_i d_i^{out} d_j^{in} q_j \rangle_e / \hat{\lambda}_Q^{(0)}. \quad (4.26)$$

Now defining a new assortativity coefficient appropriate to networks with heterogeneous biases q_i , we write

$$\rho_Q = \frac{\langle q_i d_i^{out} d_j^{in} q_j \rangle_e}{\langle q_i d_i^{out} \rangle_e \langle q_j d_j^{in} \rangle_e} = \frac{\langle q_i d_i^{out} d_j^{in} q_j \rangle_e}{(\hat{\lambda}_Q^{(0)})^2}, \quad (4.27)$$

in terms of which Eq. (4.26) takes the suggestive form,

$$\hat{\lambda}_Q \approx \hat{\lambda}_Q^{(0)} \rho_Q. \quad (4.28)$$

Thus bias assortativity (disassortativity), corresponding to $\rho_Q > 1$ ($\rho_Q < 1$) yields $\hat{\lambda}_Q > \hat{\lambda}_Q^{(0)}$ ($\hat{\lambda}_Q < \hat{\lambda}_Q^{(0)}$). Equations (4.27) and (4.28) generalize Eqs. (4.2) and (4.4) for λ_A to results for λ_Q .

4.3.3 Community and Bipartite Structure

We now consider how the presence of several network groups ($s > 1$) influence $\hat{\lambda}_Q$. As in Sec. 4.3.1, we assume that \underline{z}_i is uncorrelated with \underline{z}_j , where \underline{z}_i and \underline{z}_j are at either end of a link from i to j . However, we do include correlations between σ_i and σ_j along this link, and we characterize this correlation by the $s \times s$ matrix of transition probabilities $p_{\sigma\sigma'}$, giving the probability that a randomly chosen out-link from a node in group σ' connects to a node in group σ . With these assumptions, we have the following result for $\Pi(\underline{z}, \sigma | \underline{z}', \sigma')$ (analogous to (4.14)),

$$\Pi(\underline{z}, \sigma | \underline{z}', \sigma') = D^{-1}(\sigma') p_{\sigma\sigma'} d^{in} P_{\sigma}(\underline{z}), \quad (4.29)$$

where $D(\sigma') = \sum_{\underline{z}, \sigma} P_{\sigma}(\underline{z}) d^{in} p_{\sigma\sigma'}$ is a normalizing factor (see Eq. (4.11)). Inserting (4.29) into (4.13),

$$\hat{\lambda}_Q v(\underline{z}, \sigma) = q \sum_{\sigma', \underline{z}'} D^{-1}(\sigma') d^{in} p_{\sigma\sigma'} P_{\sigma}(\underline{z}) (d^{out})' v(\underline{z}', \sigma'). \quad (4.30)$$

Equation (4.30) immediately determines the \underline{z} dependence of $v(\underline{z}, \sigma)$. Thus we can write

$$v(\underline{z}, \sigma) = q d^{in} P_{\sigma}(\underline{z}) w(\sigma), \quad (4.31)$$

where the σ dependent quantity $w(\sigma)$ is, as yet, undetermined. Substituting (4.31) into (4.30) we obtain the following eigenvalue equation for $w(\sigma)$ and $\hat{\lambda}_Q$,

$$\hat{\lambda}_Q w(\sigma) = \sum_{\sigma'} M_{\sigma\sigma'} w(\sigma'), \quad (4.32)$$

where M is the $s \times s$ matrix,

$$M_{\sigma\sigma'} = D^{-1}(\sigma') \langle qd^{in} d^{out} \rangle_{\sigma'} p_{\sigma\sigma'}, \quad (4.33)$$

where $\langle \cdot \rangle_{\sigma} = \sum_{\underline{z}} (\cdot) P_{\sigma}(\underline{z})$. Thus the $N \times N$ eigenvalue problem for λ_Q is now approximated by the much smaller $s \times s$ eigenvalue problem (4.32),

$$\hat{\lambda}_Q = \max. \text{ eigenvalue}[M]. \quad (4.34)$$

We have also expanded the group eigenvalue problem to obtain the correction to (4.34) that is introduced by including correlations between \underline{z}_i and \underline{z}_j along links from j to i . This analysis proceeds in a manner similar to that in Sec. 4.3.2 and is omitted.

Note that in the case where the off-diagonal transition probabilities are zero, $p_{\sigma\sigma'} = 0$ for $\sigma \neq \sigma'$, we have s completely disconnected groups, and that, for $p_{\sigma\sigma'}/N_{\sigma}$ independent of σ and σ' , the group-dependence on the connectivity is absent. If the diagonal terms of the matrix $p_{\sigma\sigma'}/N_{\sigma}$ are larger than the off-diagonal terms, then we say there is ‘community structure’ (i.e., the density of intragroup connections is larger than the density of intergroup connections).

At the opposite extreme, for the case of two groups ($s = 2$), if the diagonal components of the transition probability matrix are zero ($p_{\sigma\sigma} = 0$ for $\sigma = 1, 2$), then connections exist only between, and not within, the two groups, i.e., the network is

‘bipartite.’ Thus, if the diagonal terms of the matrix $p_{\sigma\sigma'}/N_\sigma$ are smaller than the off-diagonal terms, then we say the network has ‘bipartite structure.’

In our numerical tests of Eq. (4.34) in Sec. (4.4.3), we will consider two groups ($s = 2; \sigma = 1, 2$) with equal sizes ($N_1 = N_2 = N/2$) and with symmetric transition properties ($p_{11} = p_{22} \equiv p_0$, $p_{12} = p_{21} \equiv p_x$). We will, in addition, restrict our consideration to the case where the in-degree/out-degree distributions are the same for the two groups, but we will allow the biases q for the two groups to be unequal, with the q ’s not correlated with d^{in} and d^{out} ; i.e.,

$$P_\sigma(\underline{z}) = P^d(d^{in}, d^{out})P_\sigma^q(q). \quad (4.35)$$

With these conditions Eq. (4.34) reduces to

$$M_{\sigma\sigma'} = \langle q \rangle_{\sigma'} \xi p_{\sigma\sigma'}, \quad (4.36)$$

where

$$\xi = D^{-1}(1)\langle d^{in} d^{out} \rangle_1 = D^{-1}(2)\langle d^{in} d^{out} \rangle_2, \quad (4.37)$$

or

$$M = \xi \begin{bmatrix} p_0 \langle q \rangle_1 & p_x \langle q \rangle_1 \\ p_x \langle q \rangle_2 & p_0 \langle q \rangle_2 \end{bmatrix}. \quad (4.38)$$

From Eqs. (4.34) and (4.38),

$$\hat{\lambda}_Q = \xi \left\{ p_0(\langle q \rangle_1 + \langle q \rangle_2) + [p_0(\langle q \rangle_1 - \langle q \rangle_2)^2 + 4p_x \langle q \rangle_1 \langle q \rangle_2]^{1/2} \right\} / 2. \quad (4.39)$$

Equation (4.39) can be put in a somewhat more revealing form by introducing $q_\pm = (\langle q \rangle_1 \pm \langle q \rangle_2)/2$, in terms of which (4.39) becomes

$$\hat{\lambda}_Q = \xi \left\{ p_0 q_+ + [(p_0^2 - p_x^2) q_-^2 + p_x^2 q_+^2]^{1/2} \right\}. \quad (4.40)$$

From (4.40) we see that, if we keep q_+ (the average q value for the whole network) fixed, but allow the difference between the average q 's in the two groups to increase (i.e., we increase $|q_-|$), then $\hat{\lambda}_Q$ increases if the network has community structure ($p_0 > p_x$), but it decreases if the network has bipartite structure ($p_x > p_0$).

4.4 Numerical Tests

4.4.1 First-order Approximation

We test the predictions of Eq. (4.17) on networks with equal power-law in-degree and out-degree distributions. To construct the networks used to test this hypothesis, we follow the method used in [69]. In particular, we first randomly construct a list of N degree values by choosing N random numbers drawn from a given distribution, in this case,

$$P(d) \propto \begin{cases} d^{-\gamma}, & d^{\min} \leq d \leq d^{\max}, \\ 0, & \text{otherwise.} \end{cases} \quad (4.41)$$

We use $\gamma = 2.5$ and adjust d^{\min} and d^{\max} to tune $\langle d \rangle$. We then assign each number on this list to each node i and we call this assignment the ‘target’ in-degree \hat{d}_i^{in} . Next we use this same list to assign to each node i a target out-degree \hat{d}_i^{out} , and perform this assignment in one of three ways: (i) $\hat{d}_i^{\text{out}} = \hat{d}_i^{\text{in}}$, yielding maximal $\langle d^{\text{in}} d^{\text{out}} \rangle$ and η ; (ii) \hat{d}_i^{out} randomly drawn from the list, yielding $\langle d^{\text{in}} d^{\text{out}} \rangle \approx \langle d \rangle^2$ and $\eta \approx 1$; or (iii) the node with the largest \hat{d}_i^{in} is assigned \hat{d}_i^{out} equal to the smallest value on the list, the node with the second largest \hat{d}_i^{in} is assigned \hat{d}_i^{out} equal to the second smallest value on the list, etc., yielding minimal $\langle d^{\text{in}} d^{\text{out}} \rangle$ and η . Once the \hat{d}_i^{in} and

\hat{d}^{out} are assigned, we construct the network by setting the elements of the adjacency matrix $A_{ij} = 1$ with probability $\hat{d}_i^{in}\hat{d}_j^{out}/N\langle\hat{d}\rangle$ (where $\langle\hat{d}\rangle = \langle d \rangle$ is the average of the list values) and 0 otherwise.

After the network is constructed, we assign the biases q_i drawn from a uniform distribution on the interval $[0, 1]$. For each of the three values of $\langle d^{in}d^{out} \rangle$, we tune $\langle qd^{in}d^{out} \rangle$ by swapping the biases of random pairs of nodes to increase or decrease $\langle qd^{in}d^{out} \rangle$. For example, if we wish to obtain increased $\langle qd^{in}d^{out} \rangle$, we only keep those swaps that increase $\langle qd^{in}d^{out} \rangle$. In Fig. 4.1, we plot the measured normalized eigenvalue $\lambda_Q/\langle d \rangle$ vs. $\langle qd^{in}d^{out} \rangle/\langle d \rangle^2$ for $\langle d \rangle \approx 10$ (open markers) and $\langle d \rangle \approx 100$ (filled markers) for $\langle d^{in}d^{out} \rangle$ maximal (circles), minimal (squares), and neutral (triangles) averaged over 10 networks. As can be seen, the markers all fall on the solid line, $\lambda_Q/\langle d \rangle = \langle qd^{in}d^{out} \rangle/\langle d \rangle^2$.

4.4.2 Assortativity

In Fig. 4.2 we test the predictions of Eq. (4.28). Baseline networks of size $N = 10^4$ with $\eta \approx 1$ and $\rho \approx 1$ are constructed as described above, with the biases q_i drawn from a uniform distribution on the interval $[0, 1]$. We then consider two methods of tuning ρ_Q , method (a), which yields networks with $\rho_Q \neq 1$ but no correlation between the degrees and the bias at a given node, and method (b), which introduces nodal degree-bias correlations.

Method (a). This method is a modified version of the algorithm in [69]:

(i) Randomly choose two links going from $j_1 \rightarrow i_1$ and $j_2 \rightarrow i_2$. (ii) Calculate

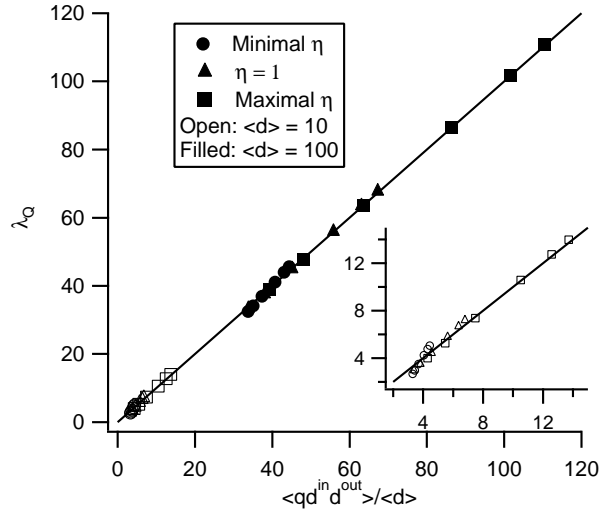


Figure 4.1: $\lambda_Q / \langle d \rangle$ vs. $\langle qd^{in}d^{out} \rangle / \langle d \rangle^2$ for networks of size $N = 10^4$ with no assortativity and $\langle d \rangle = 100$ (filled markers) and $\langle d \rangle = 10$ (open markers). For both values of $\langle d \rangle$, three values of η are considered: maximal (circle), neutral (triangle) and minimal (squares). Each marker is the average of 10 networks, and the solid line is the theoretical prediction, $\lambda_Q / \langle d \rangle = \langle qd^{in}d^{out} \rangle / \langle d \rangle^2$.

$d_{j_1}^{in} d_{i_1}^{out} q_{j_1} q_{i_1} + d_{j_2}^{in} d_{i_2}^{out} q_{j_2} q_{i_2}$ and $d_{j_1}^{in} d_{i_2}^{out} q_{j_1} q_{i_2} + d_{j_2}^{in} d_{i_1}^{out} q_{j_2} q_{i_1}$. (iii) If the latter value is larger or smaller (depending on whether the target ρ_Q is greater or less than one), delete the original links and place new links from $j_1 \rightarrow i_2$ and $j_2 \rightarrow i_1$, otherwise keep the original links. (iv) Repeat this process until the target ρ_Q is achieved.

Method (b). This method is a two-step process. First, we tune ρ by swapping inputs of random link pairs, and we do this without regard to the node biases, as in [69], yielding a network with $\rho_Q \approx \rho$. Once ρ is tuned, we further tune the bias assortativity ρ_Q by the following: (i) Randomly choose two nodes, i and j . (ii) Calculate the change in ρ_Q that would result if the q 's at these two randomly chosen nodes were interchanged. (iii) If it is desired to increase (decrease) ρ_Q and the change in ρ_Q is positive (negative), then swap the q values; otherwise do not make the swap. (iv) Repeat the above process until the target ρ_Q is achieved.

The results of these two methods are in Fig. 4.2. Each marker in the figure is the average of 10 networks of size $N = 10^4$, and we consider networks with $\langle d \rangle = 10$ (open markers) and $\langle d \rangle = 100$ (filled markers) tuned with both methods. In Fig. 4.2(a), we plot the normalized eigenvalue $\lambda_Q/\langle d \rangle$ vs. ρ_Q for networks tuned with method (a). Since η is approximately unity and the q_i are assigned independently of the node degrees, $\hat{\lambda}_Q^{(0)} \approx \langle d \rangle \langle q \rangle$; the theoretical prediction (solid curve) is therefore $\hat{\lambda}_Q/\langle d \rangle = \rho_Q \langle q \rangle$. The results of method (b) are shown in Fig. 4.2(b). We consider networks tuned to $\rho \approx 0.8$ (circles), 1.0 (triangles), and 1.2 (squares). Note that swapping the q values in method (b) changes $\hat{\lambda}_Q^{(0)}$ as well as ρ_Q , and thus $\hat{\lambda}_Q^{(0)}$ must be calculated for every marker. We therefore plot $\lambda_Q/\langle d \rangle$ vs. $\hat{\lambda}_Q^{(0)} \rho_Q/\langle d \rangle$, and we see that all the points fall on the theoretical prediction, $\lambda_Q/\langle d \rangle = \hat{\lambda}_Q^{(0)} \rho_Q/\langle d \rangle$.

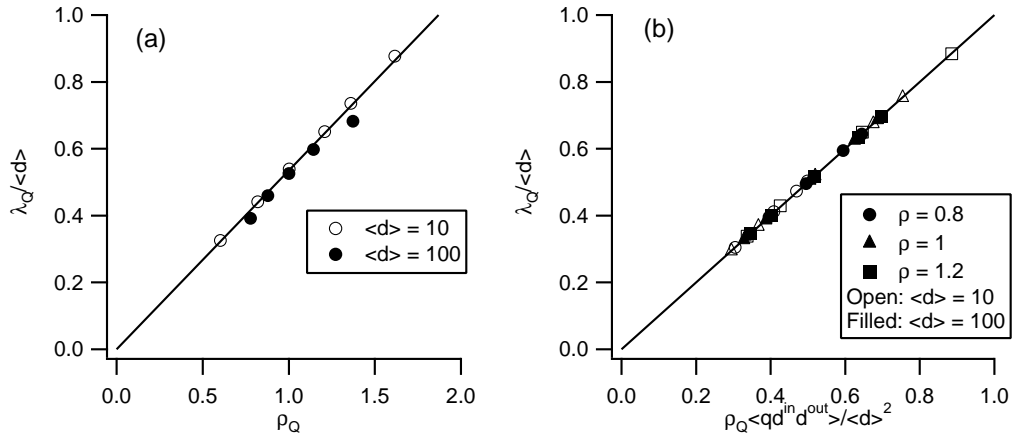


Figure 4.2: (a) $\lambda_Q / \langle d \rangle$ vs. ρ_Q for a network of size $N = 10000$ and average connectivity $\langle d \rangle = 10$ (circles) and $\langle d \rangle = 100$ (squares). Each marker is the average of 10 networks. (b) $\lambda_Q / \langle d \rangle$ vs. $\hat{\lambda}_Q^{(0)} \rho_Q / \langle d \rangle$ for networks with structural assortativity of 0.8 (circles), 1.0 (triangles), and 1.2 (squares) of size $N = 10000$ and average connectivity $\langle d \rangle = 10$ (open markers) and $\langle d \rangle = 100$ (filled markers).

4.4.3 Community Structure

In Fig. 4.3 we test the predictions of the community structure theory for a network of size $N = 10^4$ with two equally sized groups. Networks are constructed as described Sec. 4.3.3; $A_{ij} = 1$ with probability p_0 if j and i are in the same group or probability p_x if i and j are in different groups. We then consider four cases: two completely separated components ($p_x = 0$, circles), strong community structure ($p_x = p_0/2$, squares), no group structure ($p_x = p_0$, upward pointing triangles), and strong bipartite structure ($p_x = 2p_0$, downward pointing triangles). The groups have uniform biases, $q_1 = q_+ + q_-$ and $q_2 = q_+ - q_-$, with $q_+ = 0.5$ and q_- varying from 0 to 0.5. We plot the measured λ_Q vs. the difference in group biases, q_- , averaged over 10 networks. The solid curves are the theoretical predictions of Eq. (4.40), and markers are the average of 10 networks.

Again we obtain excellent agreement between the theory and the numerical tests. Note that, as mentioned in Sec. 4.3.3, the effect of increasing q_- is to increase λ_Q in the case with community structure and to decrease λ_Q in the case with bipartite structure.

4.5 Conclusion

Motivated by recent work on the stability of gene network models [85] and on percolation on directed networks [66], we have developed and numerically tested theoretical predictions for the maximum eigenvalues λ_Q of the modified adjacency matrix Q defined by Eq. (4.5). Using a Markov network model (Sec. 4.2), we

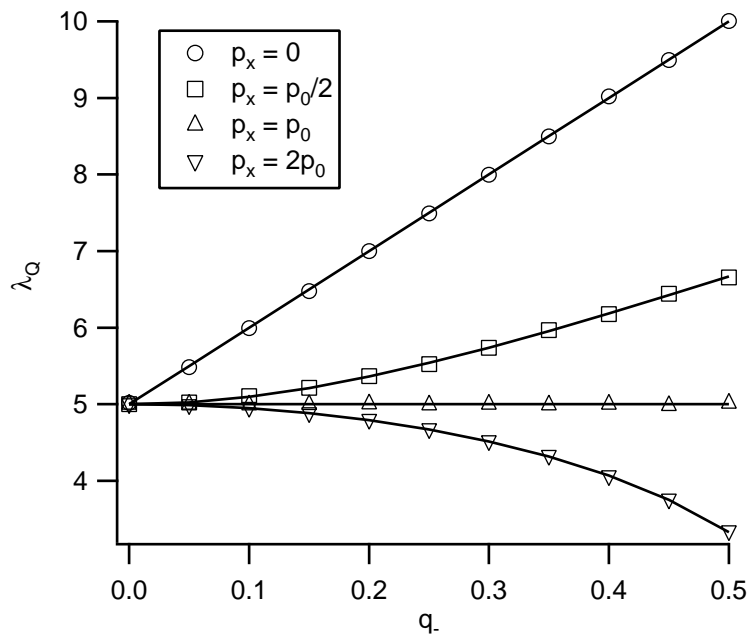


Figure 4.3: λ_Q vs. q_- for networks of size $N = 10^4$ with two equal groups of varying type: two completely separated components ($p_x = 0$, circles), strong community structure ($p_x = p_0/2$, squares), no group structure ($p_x = p_0$, upward pointing triangle), and strong bipartite structure ($p_x = 2p_0$, downward pointing triangle). Each marker is the average of 10 networks, and the solid curves are the theoretical predictions of Eq. (4.40).

calculate approximations to λ_Q for various situations (Sec. 4.3). In particular, we considered: (i) the effect of correlation between the bias q at a node with the product $d^{in}d^{out}$ at that node; (ii) the effect of correlations between the degrees and biases for nodes at the two ends of a network link; and (iii) the effect of the existence of groups of nodes with community or bipartite structure in which different node bias distributions apply to different groups. We find that the effects discussed strongly influence the value of λ_Q , and in all cases our numerical tests (Sec. 4.4) resulted in excellent agreement with our theoretical results.

This work was supported by NSF (Physics) and by ONR (contract N00014-07-1-0734). The work of A.P. was partly supported by the NCI intramural program.

Appendix A

Actin Purification

As outlined in Chapter 1, there are three phases to actin purification from rabbit muscle. This Appendix will detail the final two phases as muscle acetone powder is commercially available.

A.1 Extracting Polymerized Actin

Actin is extracted into a buffer known as Buffer A, which consists of 4 mM Tris, 0.2 mM CaCl₂, 0.2 mM Na₂ATP, 0.005% NaN₃, DTT 0.5 mM, and pH 8.0.

Actin in muscle acetone powder is extracted by the following steps:

1. 10 g muscle acetone powder is stirred with 200 mL Buffer A for 30 minutes to dissolve actin into the buffer.
2. The mixture is filtered through cheesecloth and the liquid containing actin is retained.
3. The acetone powder is stirred again in 150 mL of fresh buffer A for 30 minutes.
4. The mixture is filtered through cheesecloth and the liquid is pooled with the result from step 2, yielding 350 mL of actin in Buffer A.
5. The liquid is centrifuged at 10,000 rpm at 4 degrees C for 1 hr and filtered through cheesecloth in order to remove small pieces of acetone powder.

6. The actin in the supernatant is polymerized by addition of 50 mM KCl and 2 mM MgCl₂ and allowed to sit at least 2 hours at 4 degrees C.
7. Polymerized actin is stirred with 0.55 M KCl for 30 mins.
8. The polymerized actin is centrifuged at 52,000 rpm and 4 degrees C for 1.5 hr in order to spin the actin filaments out of solution, leaving impurities in solution.
9. The pellets containing near-solid actin are collected and homogenized in fresh buffer A, and centrifuged again at 52,000 rpm.
10. The pellets are collected and allowed to soak in Buffer A for at least six hours.
11. The pellets are then homogenized and the result is concentrated polymerized actin.

The polymerized actin that results from this process is stable and can be stored on ice for up to 2 months.

A.2 Depolymerization and Final Purification

The polymerized actin from the previous phase is then depolymerized by dialyzing against Buffer A for 4 days. The Buffer A is replaced five times throughout the dialysis phase. At the end of the dialysis, the resulting solution is eluted through a Sephadex gel column and fractionated. Fractions containing actin (as determined by staining with Coomassie Blue) are pooled, and the concentration is measured by

spectrophotometer, using $0.63 \text{ cm}^{-1} \text{ mL/mg}$ as the extinction coefficient at 290 nm and subtraction of the absorption at 330 nm to account for background.

Appendix B

Overview of Microscopy and Image Processing Techniques

In this Appendix, we give some background on the two microscopy techniques and the methods of interpreting the resulting images used in Chapter 2, laser tweezers and spinning disk confocal microscopy. In the case of laser tweezers, we spend some time considering the drawbacks of holographic laser tweezers, which prevented performing corroborating measurements.

B.1 Laser Tweezers

B.1.1 General Principles

Initial observations of interactions between laser beams and micron-sized particles were first reported by Ashkin in 1970, and by 1986 he developed a technique by which small dielectric particles to be manipulated by tightly focused laser beams [90]. In the case where the index of refraction of the object is higher than the surrounding medium, the object is drawn into the focus of the beam; in the case where the object has lower index of refraction than the medium, the object is repelled from the focus.

In the cases of relevance to this dissertation, the trapped particle is significantly larger than the wavelength of the trapping beam, a ray optics explanation suffices for lateral trapping, which is illustrated in Fig B.1. When the light beam

impinges on the bead, the difference in indices of refraction causes the beam to refract. This reflection changes the direction of the light beams and, concomitantly, the momentum carried by the light. Due to conservation of momentum, the bead feels a force in the direction opposite of the deflection. When the input beam is Gaussian and the object has higher index of refraction, the force due to refracting light in the center of the beam is stronger than that at the periphery; thus there is a net force toward the center of the beam if the object is off-axis. When the object is in the center of the beam, there is no net lateral force due to refraction. In the direction of propagation, there are two forces: scattering forces which tend to push the object in the direction of propagation, and gradient forces which tend to pull the object into the focus of the beam. If the numerical aperture of the beam is high enough, the gradient forces can balance the scattering forces and stable trapping can occur; otherwise, the object is pushed out of the trap in the direction of propagation.

One important use of laser tweezers is force measurement. If the trapped object has an equilibrium position outside the center of the trap, there must be a force moving it there. By measuring the displacement from the center of the trap, the force can be measured (given suitable calibration, of course). This would be a useful measurement for the actin experiments described in Chapter 2, however the apparatus on which the experiments were performed, a holographic laser tweezer system, this is not possible. However, the confocal microscope is well-suited to these measurements, and they will appear in the paper to be published with our collaborators.

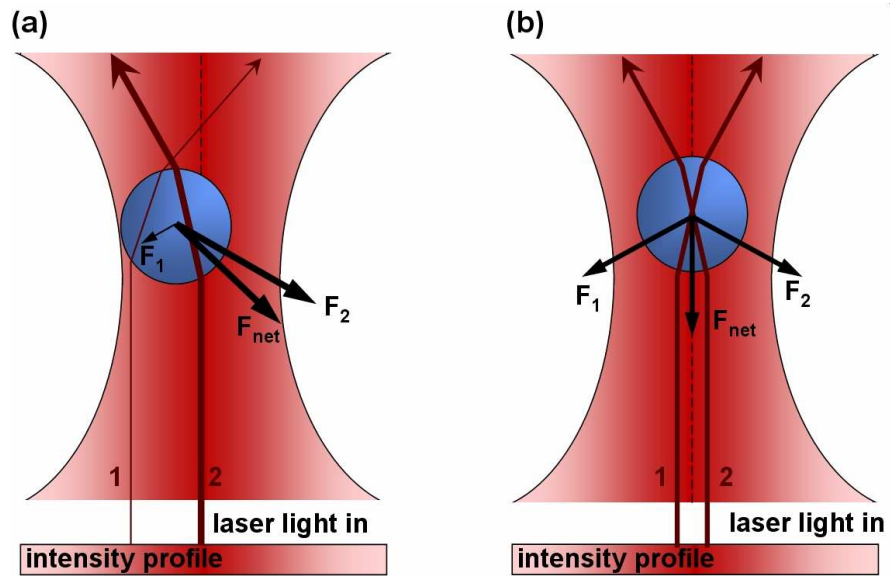


Figure B.1: Illustration of lateral optical trapping. (a) When the particle is displaced in the trap to the left, the force resulting from refracting light to the right, F_1 , is smaller than the force resulting from refracting light to the left, F_2 . The result is a net restoring force to the right, F_{net} . (b) When the particle is in the center of the trap, F_1 and F_2 balance each other, so that the net force is down, which is balanced by radiation pressure. Image courtesy Wikipedia entry on Optical Tweezers.

B.1.2 Holographic Laser Tweezers

While laser tweezers are a very powerful tool for manipulating micron-sized objects, one significant drawback is that (without sophisticated techniques that have their own shortcomings) each laser trap requires its own laser, and that it becomes increasingly difficult to send multiple lasers through the same microscope objective. One solution to this problem is holographic laser tweezers, (or holographic optical trapping, abbreviated HOT). In this technique, a spatial light modulator (SLM) is placed in the beam path. An SLM is a device composed of a two-dimensional array of devices that modulate the phase of incoming light. Each of the devices is independently programmable, so that it can impose an image on the reflected light. HOT uses the SLM to impose an image that, in the focal plane of the microscope, appears to be a set of tightly focused Gaussian beams capable of trapping, as above. Thus, in principle, a single beam can be split into any number of independently movable traps.

However, there are some serious drawbacks to holographic optical trapping which render it unsuitable for force measurement. The first is that the beam profile of a trap is very distorted due to the necessary discretization and quantization of the SLM device. Additionally, the beam profiles can be very sensitive to the absolute position of the trap and to the relative positions of an array of traps. Thus, an accurate force measurement is only possible if the calibration occurs for every array of traps used in the experiment. While this is not impossible, it becomes prohibitively difficult if a large number of traps are used that move relative to one

another.

The more serious problem for the purposes of these experiments relates to the method by which traps are moved. In a typical laser tweezer setup, a trap can be moved by moving the mirror that carries the beam into the microscope; in this way the beam, with approximately constant profile, is smoothly moved in the image plane. However, in HOT, the traps move discretely, where the SLM presents a series of images that move the trap in a series of steps. Due to the operation of the SLM, this in fact leads to the following: (1) a trap is currently on, (2) the trap turns off for a finite time, and (3) the trap turns back on in a different location. The turn-on and turn-off of the trap each carry their own complications, such that it is impractical to attempt force measurements with moving traps.

Despite these drawbacks, HOT can be extremely useful for applying strain (i.e., known position) in multiple positions to a sample (and it has been used in [89] in the lab for this), but it is completely unsuited to stress-controlled (i.e., constant force) experiments.

B.2 Confocal Microscopy

Confocal microscopy is a general technique for improving the contrast and spatial resolution of fluorescence microscopy. In fluorescence microscopy, an excitation beam (usually a suitably filtered sodium lamp or laser beam) is sent into the sample which excites fluorescent molecules that emit photons of a higher wavelength. However, the naive implementation allows significant out-of-focus fluorescent light

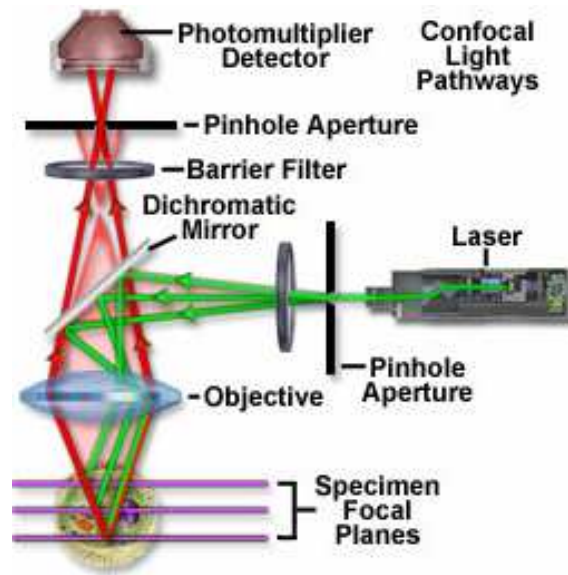


Figure B.2: Schematic beam path in a confocal microscope. The laser illuminates the sample, which excites fluorescence by the probes in the sample. The fluorescent light is collected by the object and focused. However, some of the fluorescent light is emitted by probes outside the focal plane. This light is blocked by a pinhole aperture in front of the photomultiplier tube, which detects the light. Image courtesy Olympus Corporation, <http://www.olympusfluoview.com/theory/index.html>.

into the viewing plane, thus washing out the image. Confocal microscopy applies a pinhole to the incoming light, which filters the out-of-focus fluorescence. See Fig. B.2 for a schematic.

B.3 Image Analysis

B.3.1 Particle Tracking

The goal of particle tracking is, as its name implies, to track the trajectories of individual particles in a given image sequence. In order to track particles, they must either be significantly brighter or darker than their surroundings; in the case of a microscope image of silica beads, the beads appear as approximately Gaussian blobs against a gray background. John Crocker et al. [31] have developed a sensitive particle tracking software package for IDL well-suited to this problem that was used in Chapter 2. In brief, the software performs four steps. The first step is bandpass filtering step, where small-scale noise and large-scale backgrounds are subtracted from the image. The next step is a threshold, which sets dark gray areas to black, but leaves bright spots unchanged. The third step is particle identification, which attempts to fit a Gaussian blob to bright spots in the image; from this fit, the center of the blob can be calculated to 0.1 pixels under suitable conditions. In the final step, the software uses the particles identified in each frame and builds trajectories by assigning particles in subsequent frames the same label if they are closest together.

B.3.2 Particle Imaging Velocimetry

Particle imaging velocitmetry (PIV) has a slightly different focus than particle tracking. Rather than track the trajectories of individual particles, PIV attempts to track the collective motion of many particles. In this way, it attempts to calcu-

late the flow-field that best explains the collective motion of nearby particles. In fluid dynamics experiments, the particles being tracked are actual neutrally buoyant particles; in our case the particles are filaments of fluorescent actin.

The method by which PIV attempts this is rather different than particle tracking. In PIV, the image is segmented into square regions, and the algorithm attempts to find the displacement of each region such that, in the next frame, the mean squared difference of the pixel values of original region and the area that the region is displaced to is minimized. The details of this operation can be rather involved and will not be summarized here. See Ref. [38] for details on the implementation used in Chapter 2.

Appendix C

Technical Notes on Boolean Networks

C.1 Transient Evolution

Figure C.1 shows the time evolution results for networks of type (a) (i.e., $K_i^{in} = K_i^{out}$ for all i and uniform $q_i = q$). Once a random network is generated, we simulate the evolution of two close initial conditions and plot the Hamming distance as a function of time in Fig. C.1. Specifically, we take an arbitrary initial condition and generate a perturbed initial condition by flipping a fraction ϵ of the state bits; in Fig. C.1, $\epsilon = 0.01$ and $N = 1000$ corresponding to 10 flipped bits. Figure C.1(a) shows the Hamming distance as a function of time step t for four cases with different values of sensitivity ($q = 0.5, 0.4, 0.3, 0.2$) and uniform delays $\tau_{ij} = 1$ (as in Eq. [4]). Each of these four curves are generated using the same network of interconnections (for which $\lambda = 4.3$) and the same perturbation in initial conditions averaged over 100 realizations of the nodal truth tables. For the three cases $q = 0.5, 0.4, 0.3$, $\lambda q = q\lambda > 1$, the network is predicted to be unstable. We see in Fig. C.1(a) that in these cases, the Hamming distance rises and eventually saturates at a constant value. In the fourth case, $q = 0.215$ and we have that $q\lambda < 1$, and the network is predicted to be stable, which is demonstrated in the figure. These cases illustrate the strong effect that in-/out-degree correlations can have: for the value $\langle K \rangle = 1.89$ in the network of Fig. C.1, the prediction from the result for uncorrelated networks,

Eq. [1], is stability for all values of q (the minimum value of $1/q$, the right hand side of [1], is 2, which exceeds $\langle K \rangle = 1.89$). Figure C.1(b) shows time traces of the Hamming distance for $q = 0.5$ when non-uniform delays are present. In the curves shown, a fraction $T = 0, 0.1, 0.5$ of the links are randomly chosen and given delays of $\tau_{ij} = 10$ with the remaining links having delay $\tau_{ij} = 1$. The curves are for the same network as in Fig. C.1(a) with $q = 0.5$ and are again the average of 100 different realization of the truth table. (The choice of delayed links is the same for all 100 realizations.) In each case, we see that the network is unstable and the Hamming distance rises to the same steady-state value, albeit at a slower rate for larger T . This result thus is consistent with our prediction that whether or not a network is stable and its final saturation value do not depend on heterogeneity of the delays.

C.2 Finite-Size Effects

In Fig. C.2(a) and (b), we consider the importance of finite-size effects by varying ϵ (a parameter which does not appear in the theory) for two different size networks of type (a). Figure C.2(a) also compares the results of simulating the frozen case (solid markers) to the semi-annealed case described in the Theory section (open markers) for $N = 10^3$. As before, in simulating a semi-annealed network, at each time step the nodal truth tables are randomly generated with the same q . The networks under consideration in Figs. C.2(a)-(b) have $T = 0$, $\lambda \approx 5.0$, and (a) $N = 10^3$ and (b) $N = 10^4$. As the figure demonstrates, larger ϵ yields better agreement with the theory, and the semi-annealed case seems indistinguishable from the frozen

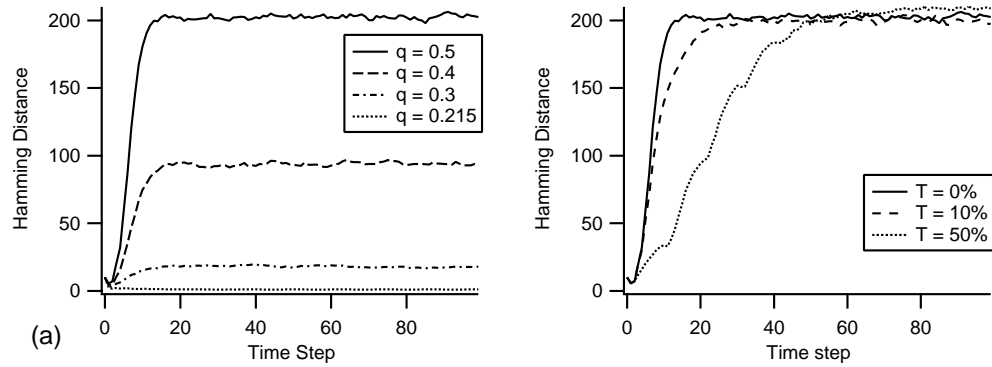


Figure C.1: (a) Evolution of the Hamming distance between two initial conditions for a typical network of size $N = 1000$ and $\epsilon = 0.01$ for various values of the sensitivity and uniform delay $\tau_{ij} = 1$. (b) Evolution of the Hamming distance between two initial conditions for a typical network of size $N = 1000$, $q = 0.5$, and $\epsilon = 0.01$. Results are shown for a network with $\tau_{ij} = 1$ for all links (solid curve) and with $\tau_{ij} = 10$ on 0.1 (dashed curve) and 0.5 (dotted curve) of the links.

case. Note also that the results for $\epsilon = 0.01$ ($\epsilon = 10^{-3}$) and $N = 10^3$ is similar to that for $\epsilon = 10^{-3}$ ($\epsilon = 10^{-4}$) and $N = 10^4$, suggesting that the relevant quantity is ϵN , the number of flipped states. The inset of Fig. C.2(a) shows the histogram of the Hamming distances used in calculating the point $q = 0.4$, $\epsilon = 0.01$ (upward vertical arrow). The different trials used in generating this histogram correspond to different truth table realizations. The distribution shown in the inset consists of a large number of samples with Hamming distance zero and a roughly symmetric part that has a mean near the theoretical prediction. The overestimation of the mean by the theory therefore seems to be driven by the relative number of zero samples compared to the symmetric part.

In order to understand the origin of the zero samples, we note that one way that they can arise is through ‘irrelevant’ nodes (i.e., nodes that do not influence the dynamics of the network) and ‘frozen’ nodes (i.e., nodes whose output is independent of its inputs due to the random assignment of the truth table). Irrelevant nodes can arise by either having no out-going links or by inputting only to other irrelevant or frozen nodes. Flipping the value of an irrelevant node, by definition, does not change the subsequent evolution of the network; if a perturbation between nearby initial conditions consists solely of such flips, that perturbation dies out quickly. Assuming that the fraction of irrelevant nodes is independent of N , then the probability that all ϵN nodes for which the two initial conditions differ are irrelevant goes to zero as $N \rightarrow \infty$ for constant ϵ ; in this case, the observations should exactly match the theoretical prediction. This is consistent with the trend indicated by our comparison of the $N = 10^3$ network in Fig. C.2(a) with the $N = 10^4$ network in Fig. C.2(b).

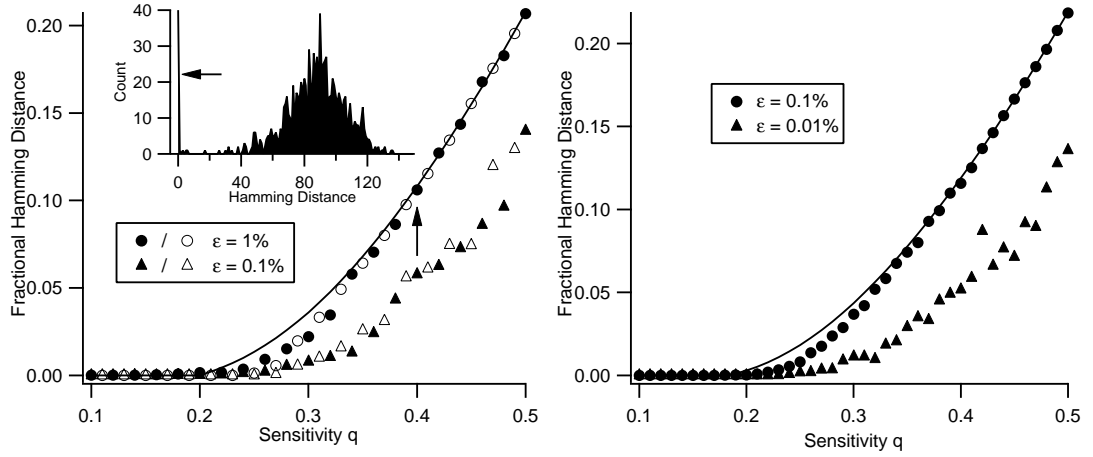


Figure C.2: The steady-state fractional Hamming distance h/N for (a) $N = 10^3$ and (b) $N = 10^4$ as a function of the sensitivity q for various values of ϵ , both in the frozen case (filled symbols) and the annealed case (open symbols). The largest eigenvalue of this network's adjacency matrix is $\lambda \approx 5$. While the theory does not depend on the value of ϵ , finite-size effects cause a dependence on the number of flipped bits. The inset to (a) shows a histogram of measured Hamming distances at $q = 0.4$ and $\epsilon = 0.01$ (up arrow).

C.3 Comparison of Mean-field Eigenvalue Approximations with Exact λ_Q

For the systems tested in our numerical experiments, Table C.1 shows the critical parameter values at the stability/instability border as obtained from direct calculation of the maximum eigenvalue of the matrix Q for the relevant specific networks (downward arrows in Fig. 3.1 (a)-(f)) compared to the corresponding results predicted from the mean-field-type theoretical estimates. For the community structure example we use the approximation,

$$\lambda_Q \approx \frac{N}{2} \left\{ \theta_{\cup} (q_a + q_b) + [\theta_{\cup}^2 (q_a - q_b)^2 + 4\theta_{\cap}^2 q_a q_b] \right\}, \quad (\text{C.1})$$

which applies for the case of two equal communities with symmetric connectivity probabilities ($\theta_{ab} = \theta_{ba} = \theta_{\cap}$, $\theta_{aa} = \theta_{bb} = \theta_{\cup}$) as in Fig. 3.1(e). The analysis leading to (C.1) will be published elsewhere.

The largest eigenvalue approximations predict the observed transition to unstable behavior quite well, as seen in the table below. The only exceptions to this agreement are in the case of significant assortativity or disassortativity; however, this is to be expected since the approximate theory is a linear approximation for values of ρ close to one. The values of assortativity and disassortativity used in the paper (1.7 and 0.5) are far from this regime. Nevertheless, even for these cases, the theory correctly predicts the qualitative trend that assortativity (disassortativity) decreases (increases) the critical q .

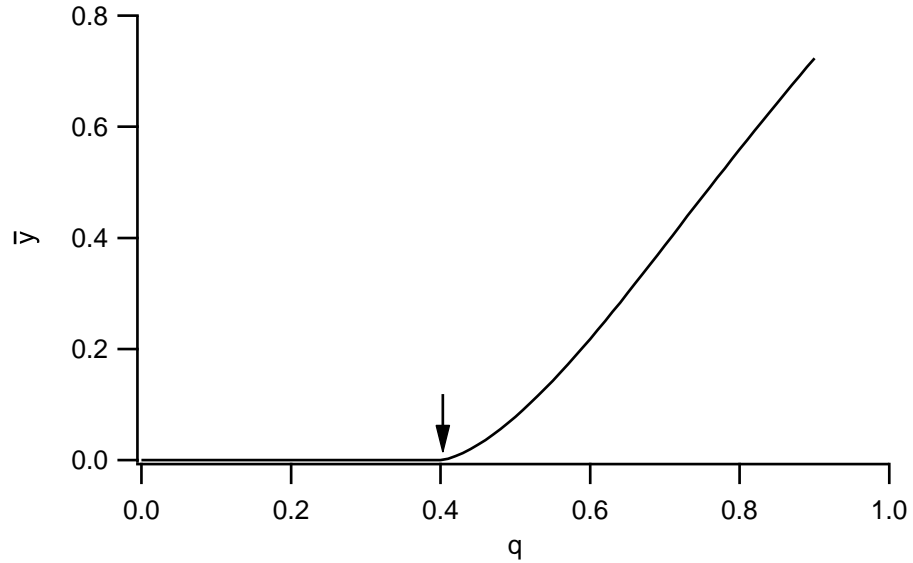


Figure C.3: $\bar{\lambda}$ vs. q , calculated from Eq. [17], for the published regulatory network of *S. cerevisiae* [35]. The network undergoes a transition from stable to unstable behavior at $q_{crit} = 1/\lambda = 0.40$.

C.4 Application to the Regulatory Network of *S. cerevisiae*

Figure C.3, similar to Figs. 3.1(a)-(c), illustrates an application of Eq. [17] to the published network of the yeast *S. cerevisiae* [35]. The largest eigenvalue of this network is $\lambda = 2.5$. We have assumed in this plot that each node has the same sensitivity q , and again we see that the network undergoes a transition from stable to unstable behavior at $q_{crit} = 1/\lambda$. However, in order to draw any conclusions about the criticality of the yeast regulatory network, we need a reliable estimate of the individual q_i 's, from which we can calculate λ_Q . While estimating the sensitivities may be possible with existing microarray datasets, this is beyond the scope of this paper.

Table C.1: Comparison between criticality conditions evaluated directly from Q and from the approximate theory.

	Direct Evaluation	Approximate Theory
Critical q 's from Fig. 1(a)	0.22	0.23
(Approx. Theory from Eq. [11])	0.34	0.34
	0.43	0.44
Critical q 's for Fig. 1(b)	0.10	0.13
(Approx. Theory from Eq. [12])	0.22	0.23
	0.33	0.45
Critical q 's for Fig. 1(c)	0.33	0.33
(Approx. Theory from Eq. [11])	0.34	0.33
	0.34	0.34
Critical q_0 for Fig. 1(d)	0.19	0.20
(Approx. Theory from Eq. [14])	0.27	0.28
Critical $\theta_n/(\theta_U + \theta_n)$ for Fig. 1(e)	0.21	0.21
(Approx. Theory from Eq. [18])		
Critical p_0 for Fig. 1(f)	0.80	0.80
(Approx. Theory from Eq. [15])		

Bibliography

- [1] C. G. Dos Remedios, D. Chhabra, M. Kekic, I. V. Dedova, M. Tsubakihara, D. A. Berry, and N. J. Nosworthy, *Physiol. Rev.* **83**, 433 (2003).
- [2] D. S. Latchman, *Int. J. Biochem. Cell Biol.* **29**, 1305 (1997).
- [3] B. Alberts and A. Johnson, *Molecular Biology of the Cell*. 2002, New York: Taylor and Francis.
- [4] Lodish, H., A. Berk, S.L. Zipursky, P. Masudaira, D. Baltimore, and J. Darnell, *Molecular Cell Biology*. 4th ed. 2000, New York: W. H. Freeman. 1084.
- [5] S. Kumar and V. M. Weaver, *Cancer Metastasis Rev* **28**, 113 (2009).
- [6] J. A. Spudich and S. J. Watt, *J. Biol. Chem.* **15**, 4866 (1971).
- [7] Rubinstein and Colby, *Polymer Physics*.
- [8] T.G. Mason and D.A. Weitz, *Phys. Rev. Lett.* **74**, 318 (1995).
- [9] John C. Crocker, M.T. Valentine, Eric R. Weeks, T. Gisler, P.D. Kaplan, A.G. Yodh, and D.A. Weitz, *Phys. Rev. Lett.* **85**, 888 (2000).
- [10] J. L. McGrath, J. H. Hartwig, and S. C. Kuo, *Biophys. J.* **79**, 3258 (2000).
- [11] M. J. Solomon and Q. Lu, *Curr. Opinion in Colloid and Interface Science* **6**, 430 (2001).
- [12] Y. Tseng, T. P. Kole, S.-H. J. Lee, and D. Wirtz, *Curr. Opinions in Colloid and Interface Science* **7**, 210 (2002).
- [13] P. A. Janmey, S. Hvidt, J. Kas, D. Lerche, A. Maggs, E. Sackmann, M. Schliwa, and T. P. J. Stossel, *J. Biol. Chem.* **51**, 32503 (1994).
- [14] B. Hinner, M. Tempel, E. Sackmann, K. Kroy, and E. Frey, *Phys. Rev. Lett.* **81**, 2614 (1998).
- [15] M. L. Gardel, M. T. Valentine, J. C. Crocker, A. R. Bausch, and D. A. Weitz, *Phys. Rev. Lett.* **91**, 158302 (2003).

- [16] A. J. Levine, and T. C. Lubensky, Phys. Rev. Lett. **85**, 1774 (2000).
- [17] F. Amblard, A. C. Maggs, B. Yurke, A. N. Pargellis, A. and S. Leibler, Phys. Rev. Lett. **77**, 4470 (1996).
- [18] J. Uhde, W. Feneberg, N. Ter-Oganessian, E. Sackmann, and A. Boulbitch, Phys. Rev. Lett. **94**, 198102 (2005).
- [19] F. Ziemann, J. Radler, and E. Sackmann, Biophys. J. **66**, 2210 (1994).
- [20] R. R. Brau, J. M. Ferrer, H. Lee, C. E. Castro, B. K. Tam, P. B. Tarsa, P. Matsudaira, M. C. Boyce, R. D. Kamm, and M. J. Lang, J. of Optics A **8**, S103 (2007).
- [21] M. L. Gardel, J. H. Shin, F. C. MacKintosh, L. Mahadevan, P. Matsudaira, and D. A. Weitz, Science **5675**, 1301 (2004).
- [22] M. Adam and M. Delsanti, Journal de Physique **44**, 1185 (1983).
- [23] P. A. Janmey, S. Hvidt, J. Kas, D. Lerche, A. Maggs, E. Sackmann, M. Schliwa, and T. P. Stossel, J. Biol. Chem. **269**, 32503 (1994).
- [24] P.A. Janmey, S. Hvidt, J. Peetermans, J. Lamb, J. Ferry, and T. Stossel, Biochem. **27**, 8218 (1988).
- [25] D. Mizuno, C. Tardin, C. F. Schmidt, and F. C. MacKintosh, Science **315**, 370 (2007).
- [26] F. C. MacKintosh, J. Ks, and P. A. Janmey, Phys. Rev. Lett. **75** 4424 (1995).
- [27] J. Uhde, N. Ter-Oganessian, D. A. Pink, E. Sackmann, and A. Boulbitch, Phys. Rev. E **72**, 061916 (2005).
- [28] H. Isambert and A. C. Maggs, Macromolecules **29**, 1036 (1996).
- [29] D. C. Morse, Macromolecules **31**, 7044 (1998).
- [30] N. Ter-Oganessian, D. A. Pink, and A. Boulbitch, Phys. Rev. E **72**, 041511 (2005).
- [31] J. C. Crocker, and D. G. Grier, J. of Colloid and Interface Science **179**, 298 (1996).

- [32] A. C. Maggs, Phys. Rev. E **57**, 2091 (1998).
- [33] R. Tharmann, M. M. A. E. Claessens, and A. R. Bausch, Biophys. J. **90**, 2622 (2006).
- [34] B. S. Chae and E. M. Furst, Langmuir **21**, 3084 (2005).
- [35] M. L. Gardel, M. T. Valentine, J. C. Crocker, A. R. Bausch, and D. A. Weitz, Phys. Rev. Lett. **91** 158302 (2003).
- [36] C. M. Waterman-Storer, A. Desai, J. C. Bulinski, and E. D. Salmon, Curr. Biol. **22**, 1227 (1998).
- [37] F. G. Schmidt, B. Hinner, and E. Sackmann, Phys. Rev. E **61**, 5646 (2000).
- [38] N. Mori and K.-A. Chang, Introduction to M-PIV (2003) (available at <http://www.oceanwave.jp/software/mpiv/>).
- [39] S. Kauffman, J. Theor. Biol. **22**, 437 (1969).
- [40] S. Kauffman, *The Origins of Order* (Oxford University Press, New York, 1993).
- [41] R. Albert and H. G. Othmer, J. of Theor. Biol. **223**, 1 (2003).
- [42] W. Coleman and G. Tsongalis, *Molecular Basis of Human Cancer* (Humana Press, 2001).
- [43] E. Ott, *Chaos in Dynamical Systems* (Cambridge University Press, 2001).
- [44] I. Gonzalez-Garcia, R. V. Sole, and J. Costa, Proc. Natl. Acad. Sci. USA **99**, 13085 (2001).
- [45] L. Bignolda, Cancer Lett. **253**, 155 (2007).
- [46] P. Rm, J. Kesselia, and O. Yli-Harjaa, J. Theor. Biol. **242**, 164 (2006).
- [47] R. Serra, M. Villani, and A. Semeria, J. Theor. Biol. **227**, 149 (2004).
- [48] M. Nykter et al., Proc. Natl. Acad. Sci. U.S.A. **105**, 1897 (2003).
- [49] A. Balleza et al., PLoS ONE **3**, e2456 (2008).

- [50] B. Derrida, and Y. Pomeau, *Europhys. Lett.* **1**, 45 (1986).
- [51] R. V. Sole and B. Luque, *Phys. Lett. A* **196**, 331 (1995).
- [52] B. Luque, and R. V. Sole, *Phys. Rev. E* **55**, 257 (1997).
- [53] J. J. Fox, and C. C. Hill, *Chaos* **11**, 809 (2001).
- [54] M. Aldana and P. Cluzel, *Proc. Natl. Acad. Sci. USA* **100**, 8710 (2003).
- [55] A. L. Barabasi and R. Albert, *Science* **286**, 509 (1999).
- [56] M. E. J. Newman, *Phys. Rev. Lett.* **89**, 208701 (2002).
- [57] M. E. J. Newman, and M. Girvan, *Phys. Rev. E* **69**, 026113 (2004).
- [58] Q. Cui et al., *Mol. Sys. Biol.* **3**, 152 (2007).
- [59] S. Maslov and K. Sneppen, *Science* **269**, 910 (2002).
- [60] E. Eisenberg and E. Y. Levanon, *Trends Genet.* **19**, 362(2003).
- [61] M. Ghil and A. Mullhaupt, *J. Stat. Phys.* **41**, 127 (1985).
- [62] K. Kappler, R. Edwards, and L. Glass, *Signal Process.* **83**, 789 (2003).
- [63] B. Luque and F. J. Ballesteros, *Physica A* **342**, 207 (2004).
- [64] I. Shmulevich and S. A. Kauffman, *Phys. Rev. Lett.* **93**, 048701 (2004).
- [65] D. S. Lee and H. Rieger, *J. Phys. A* **41**, 415001 (2008).
- [66] J. G. Restrepo, E. Ott, and B.R. Hunt, *Phys. Rev. Lett.* **100**, 058701 (2008).
- [67] R. Milo *et al.*, *Science* **298**, 824 (2002).
- [68] C. R. MacCluer, *SIAM Rev.* **42**, 487 (2000).
- [69] J. G. Restrepo, E. Ott, and B. R. Hunt, *Phys. Rev. E*, **76**, 056119 (2007).
- [70] I. Farkas, H. Jeong, T. Vicsek, A. L. Barabasi, and Z. N. Oltvai, *Physica A* **318**, 601 (2003).

- [71] M. E. J. Newman, SIAM Rev. **45**, 167 (2003).
- [72] F. Chung, L. Lu, V. Vu, Proc. Natl. Acad. Sci. USA **100**, 6313 (2003).
- [73] S. Gama-Castro, et al., Nucl. Acids. Res. **28**, D120 (2008).
- [74] I. Lee, Z. Li, E. Marcotte, PLoS ONE **2**, e988 (2007).
- [75] J. J. Faith, et al., PLoS Biol. **5**, gkm815 (2007).
- [76] A. Margolin, et al., BMC Bioinformatics **7**, S7 (2006).
- [77] J. J. Faith, et al., Nucl. Acids Res. **36**, D866 (2007).
- [78] R. Cohen, K. Erez, D. ben-Avraham and S. Havlin, Phys. Rev. Lett. **85**, 4626 (2000).
- [79] N. M. Luscombe *et al.*, Nature **431**, 308 (2004).
- [80] This definition of ρ appears in Ref. [69]. Newman [56] characterizes assortativity using a different quantity, but Eq. (4.2) is more relevant for our purposes.
- [81] M. Girvan and M. E. J. Newman, Proc. Nat. Acad. Sci. USA **99**, 8271 (2002).
- [82] E.g., see S. Boccaletti, et al. Phys. Repts. **424**, 175 (2006); L. M. Pecora and T. L. Carroll, Phys. Rev. Lett. **80**, 2109 (1998).
- [83] J. G. Restrepo, E. Ott, and B. R. Hunt, Phys. Rev. E **71**, 036151 (2005).
- [84] E. Ott, P. So, E. Barreto, and T. M. Antonsen, Physica D **173**, 29 (2002); J.G. Restrepo, E. Ott, B. R. Hunt, Phys. Rev. Lett. **96**, 254103 (2006).
- [85] A. Pomerance, E. Ott, M. Girvan, and W. Losert, to be published.
- [86] Y. Moreno, R. Pastor-Satorras, and A. Vespignani, Europhys. J. **26B**, 521 (2002).
- [87] A. Vazquez and Y. Moreno, Phys. Rev. E **67**, 015101 (R) (2003).
- [88] M. Boguñá and R. Pastor-Satorras, Phys. Rev. E **66** 04104 (2002).
- [89] A. J. Pons, A. Karma, S. Akamatsu, M. Newey, A. Pomerance, H. Singer, and W. Losert, Phys. Rev E **75**, 021602 (2007).

- [90] Ashkin, A., Dziedzic, J. M., Bjorkholm J. E, Chu, S., Opt. Lett. 11, 288-290, (1986).